Namiki *et al. Earth, Planets and Space (2018) 70:147*
https://doi.org/10.1186/s40623-018-0914-5

Earth, Planets and Space

FULL PAPER Open Access

# Physical characteristics of scoriae and ash from 2014–2015 eruption of Aso Volcano, Japan

Atsuko Namiki*, Yukie Tanaka and Tadashi Yokoyama

**Abstract**

The activity at Aso Volcano was mainly defined as a sequence of ash emissions and occasional ejections of scoria fragments with ash. Ash emissions sometimes started without notable explosions. The measured porosity of scoriae was as high as 0.94. The scoriae had a flattened shape with a low-porosity outer rim. To elucidate the eruptive conditions causing such ash emission and generation of scoriae, we conducted three series of measurements. First, we heated the high-porosity scoriae from Aso Volcano at 900–1150 °C and found that the heated scoriae shrunk by losing the gas in the bubbles. At the highest temperature, 1150 °C, bubbles segregated from the surrounding melt. Second, we conducted shear deformation experiments of scoriae and ash at 500–950 °C and found that the high-porosity scoriae easily fractured by low normal and shear stresses of $\sim 10^4$ Pa at a low temperature of 500 °C. We also found that the fine ash at a high temperature of 950 °C was sintered. Third, we measured the permeability of the sintered ash plate and unheated powder-like ash layer. The permeability of the ash plate is less than $2.5 \times 10^{-13}$ m$^2$, while that for the ash powder is greater than $10^{-11}$ m$^2$. The unheated ash particles could move in the container during the permeability measurements. This effect allowed the formation of pipe-like structures in the ash layer and increased its permeability. On the basis of these measurements, we infer the conditions inside the erupting conduit. There exists high-porosity magma foam in the conduit. The top of the magma foam is cold (<500 °C) and has a sufficiently high porosity (>0.7) to be fractured at a low stress level ($\sim 10^4$ Pa). The fractured magma foam generates the ash layer above the magma foam. The gas flow from the underlying magma foam makes the high-permeability structure in the ash layer. Eventually, the bottom of the ash layer sinters to regulate the gas flow. The pressurized magma foam breaks the sintered ash layer. The breakage at the bottom of the ash layer may not cause a notable explosion but causes ash emission. The fragmented magma foam becomes high-porosity scoriae at a high temperature, which can generate the low-porosity outer rim by shrinkage and flatted shape.

**Keywords:** Foam, Rheology, Friction, Fracturing, Permeability

## Introduction

Strombolian eruptions are frequently associated with the release of low-viscosity magma with a composition of basalt to basaltic andesite (e.g., Houghton and Gonnermann 2008; Taddeucci et al. 2015). A burst of overpressurized gas slugs has been considered as a possible mechanism for triggering major Strombolian eruptions (e.g., Blackburn et al. 1976; Chouet et al. 2003; James et al. 2009; Parfitt 2004; Ripepe 1996; Vergniolle and Gaudemer 2015). Recently, a variety of eruption styles have been reported. For instance, at Stromboli Volcano, Italy, eruption styles are classified into three types. Type 0 eruptions are gas-dominated, Type 1 eruptions are dominated by coarse ballistic clasts, and Type 2 eruptions consist of an ash-rich plume (Leduc et al. 2015; Patrick et al. 2007). Some part of the ash emitted by a Type 2 eruption falls back to the vent, which covers the vent as debris. This recycling process has also been recognized through the morphological observation of ash grains (D'Oriano et al. 2014). Reheating causes groundmass crystallization, sintering/welding, and a color change (D'Oriano et al. 2013). Such debris prevents the gas and magma flows in the conduit and may contribute to the generation of a viscous plug at a shallow conduit, which in turn affects the

*Correspondence: namiki@hiroshima-u.ac.jp
Graduate School of Integrated Arts and Sciences, Hiroshima University, 1-7-1, Kagamiyama, Higashi Hiroshima 739-8521, Japan

eruption styles (Capponi et al. 2016; Gaudin et al. 2017). Although its origin is controversial, the existence of a viscous plug has been suggested by the textural, geochemical, and rheological analysis of ejected pyroclasts and bombs (e.g., Gurioli et al. 2014; Lautze and Houghton 2007; Leduc et al. 2015).

The eruption style observed in Aso Volcano during November 2014–May 2015 is partly similar to the typical eruption styles described above, but some parts differ. In November 2014, Aso Volcano located in central Kyushu, Japan, resumed its volcanic activity from the Nakadake 1st crater (Fig. 1a–c), after an approximately 20-year quiescent period (e.g., Cigolini et al. 2018; Marumoto et al. 2017; Miyabuchi et al. 2018; Shinohara et al. 2018a; Yokoo and Miyabuchi 2015). The first half of this activity, from November 2014 to May 2015, was characterized by ash emissions and Strombolian eruption, which ejected scoriae with and without ash. The latter half, from September 2015 to February 2016, was characterized by phreatomagmatic and phreatic eruptions (Miyabuchi et al. 2018). The Nakadake 1st crater usually has hot and acid water as a crater lake, but it dried during the first half of the eruption sequence.

As we describe the details in the next section, ash emission sometimes starts without a prominent explosion. During the temporal quiescent period, a white plume rises from the vent (Fig. 1d). In some situations, the plume color gradually becomes brownish by including ash and its color turns back to whitish again. The scoriae are ejected both with and without ash (Yokoo and Miyabuchi (2015), and personal communication with A. Yokoo, Fig. 1d). These characteristics are different from what is observed for Stromboli Volcano.

Here, the eruption style of low-viscosity magma varies owing to the differences in the fluid dynamics of the magma and gas ascent and the mechanism by which the erupting magma fragments (e.g., Houghton and Gonnermann 2008). We thus infer that the ash emission observed for Aso Volcano is controlled by the recycled debris at the shallow conduit. The ash fallen back to the conduit as recycling debris may sinter, which increases the strength of the debris layer (D'Oriano et al. 2013; Vasseur et al. 2013).

The thresholds for yielding, the fracturing of the sintered debris, and the permeable gas flow within the debris layer should affect the subsequent eruption styles, and these thresholds depend on the temperature. The pre-eruptive magma temperatures estimated by Saito and co-workers (personal communication) on the basis of standard geothermometry are likely within

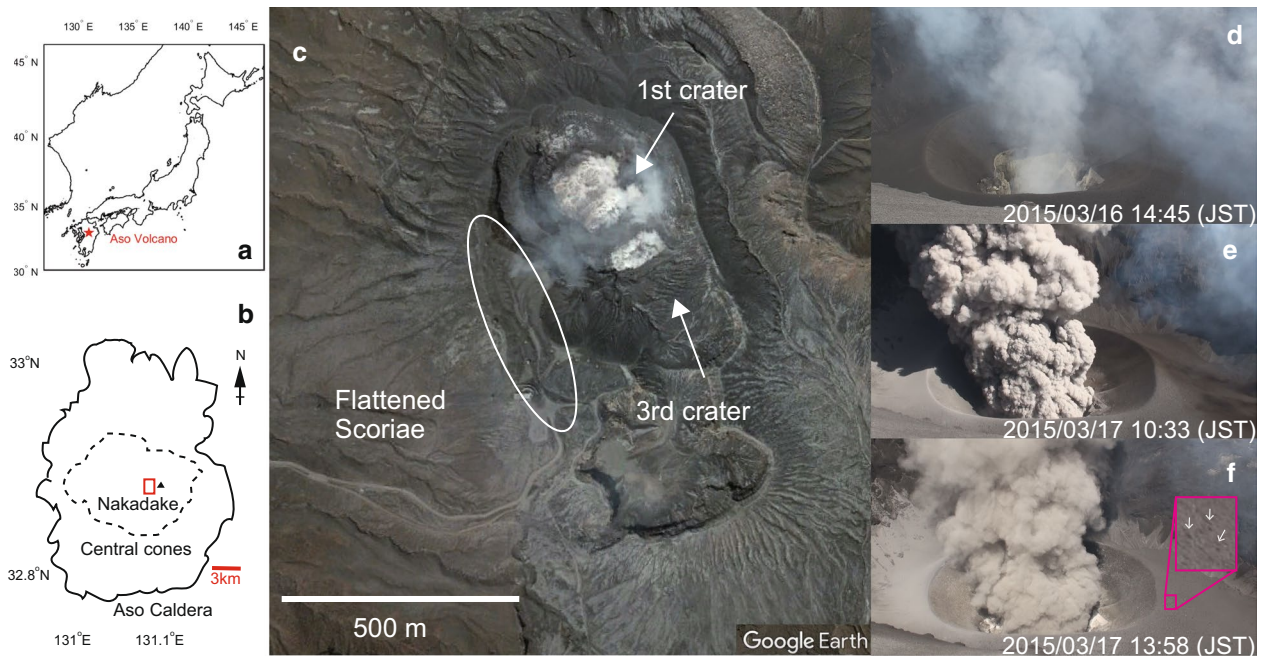


**Fig. 1** Map of Aso Volcano. **a** Location of Aso Volcano. **b** Map of Aso Caldera and Nakadake. The red square shows the location of Fig. 1c. **c** Google Earth photograph of the Nakadake craters of Aso Volcano taken April 15, 2016. High-porosity samples are collected at the 3rd crater. Flattened samples are collected around the sites denoted by the white circle. **d**–**f** Photographs of plumes without ash emission, during vigorous ash emission, and at the end of ash emission, respectively. **f** The inset shows a magnification of the sediments. The black spots denoted by white arrows are scoriae

1000–1100 °C. In this temperature range, the viscosity of the crystal-free melt is approximately $10^2$–$10^3$ Pa s (e.g., Giordano et al. 2008). On the other hand, the measured viscosity of basaltic glass is high ($> 10^9$ Pa s) (e.g., Gurioli et al. 2014; James et al. 2004). Compression experiments of basaltic ash show a large elastic modulus of $\sim 10^7$ Pa for the temperature range of 700–900 °C, and the possibility of fracturing decreases with increasing temperature (Kurokawa et al. 2017). These results show that the slight lowering of the temperature changes the viscosity, elasticity, and possibility of fracturing of the magma or debris layer. If erupted ash falls back to the conduit, the recycled ash may cool the inside of the conduit and change the eruption styles through a rheological transition.

The details of volcanic gas behavior have been revealed by gas composition measurements (Shinohara et al. 2018b). In the Nakadake crater area, the magmatic gases segregated from the melt were emitted from the vent and southern wall of the crater as a plume and fumaroles, respectively. In the quiescent period, the Nakadake 1st crater hosted a lake of hot and acid water (e.g., Terada et al. 2012). Although the lake dried prior to the beginning of the activity, the ash emissions from the dried vent sometimes included salt-shell fallouts, a product of the dried hydrothermal droplets, indicating that a hydrothermal system continuously existed beneath the dried crater floor (Shinohara et al. 2018a). The composition ratios (e.g., $CO_2/SO_2$) of the gases observed in the volcanic plume in the eruptive period varied. Interestingly, the average of the composition ratios from the lake and fumaroles in the quiescent time and that in the volcanic plume were similar. Here, the gas composition depends on the temperature and pressure conditions where the gas segregates from the surrounding magma; that is, from the measured gas composition, the apparent equilibrium conditions can be reproduced (e.g., Ohba et al. 1994; Shinohara et al. 2011). The measured composition ratios suggest that the magmatic gases from the crater lake, fumarole, and eruptions are all derived from the same source, and the variation of $CO_2/SO_2$ ratio in the eruptive period is attributed to the changes in degassing pressure. The estimated pressure range of the gas segregation from the magma during the eruptive period was 0.2–20 MPa (Shinohara et al. 2018b). Here, the estimated volume of degassed magma based on the sulfur content of the melt inclusions and $SO_2$ flux during the early 70 days of the eruptive period was $2 \times 10^8$ tons, while $2 \times 10^6$ tons of ash was emitted in the same period. That is, a large amount of magma, which brought volcanic gases, still resides underground without eruption (Shinohara et al. 2018b).

In order to understand the effect of the recycled ash on eruption styles, we need to know (1) the temperature of the erupting magma, (2) the fracturing conditions of the magma foam to be scoriae and ash, (3) the granular behavior of ash, and (4) the permeability of the ash layer. In this study, we estimate conditions (1–4) by using ejecta from Aso Volcano. First, we reheat the scoria samples and measure their volume change to estimate the possible temperature range of erupted scoriae (1). Second, we demonstrate the conditions for brittle failure and frictional behavior by deformation experiments with scoriae and ash (2–3). Third, we measure the permeability of the unheated ash powder and sintered ash plate (4). Finally, on the basis of our experimental results, we estimate the time evolution of the conditions in the conduit that vary the eruption style of Aso Volcano.

## Aso Volcano

Aso Volcano has a large caldera with dimensions of approximately 25 km in north–south direction and 18 km in east–west direction (Fig. 1b). The caldera was formed by four times of major eruptions during 270–90 ka, called Aso-1 to Aso-4 (e.g., Ono and Watanabe 1985). After the last major eruption Aso-4, several post-caldera cones formed near the center of the caldera. The composition of the cones is wide in the range from basalt to rhyolite.

Currently, Nakadake (Fig. 1c) is the only active volcano (e.g., Miyabuchi et al. 2006). Eruptions from the active crater of Nakadake were characterized by a discharge of black ash with a basaltic andesite composition (Miyabuchi et al. 2008; Ono et al. 1995). The eruption was sometimes accompanied with ejection of scoriae. The recent activities in Nakadake were observed in the 1st carter and were also characterized by ash emissions and Strombolian eruptions (Sudo 2001).

The Nakadake 1st crater usually has hot acid water, and the water level decreases with an increase in the volcanic activity (e.g., Terada et al. 2012). The water in the crater disappeared by late 2013, and eruption started on November 25, 2014 (Shinohara et al. 2018a). The typical eruption style from November 2014 to May 2015 was continuous ash eruption sometimes including scoriae. The events during November–December 2014 were vigorous. A red-hot feature was observed in the root of the ash including the plume close to the vent. The ejected scoriae also showed a red-hot feature and were elongated and toned apart on the ballistic orbit. These characteristics suggest a high temperature of the erupting magma. The event on December 9, 2014, erupted a massive amount of scoriae. The large scoriae $> 0.1$ m with a flattened shape were observed on the west side of the 1st crater (Yokoo and Miyabuchi 2015).

The composition of the scoriae was basaltic andesite (NIED et al. 2015). Some low-density scoriae have flattened shapes with a rim made of small vesicles (Fig. 2). The eruption style in the activity during 2014–2015 was similar to that reported for the former eruption (Ono et al. 1995), in which the emission of ash dominated the eruption; occasionally a frothy scoria, Pele's hair, and a glass sphere were observed.

Figure 1d–f shows typical plumes observed during March 16–17, 2015. In the quiescent time, a white plume was located in the vent (Fig. 1d). When ash emission began, the plume became brownish (Fig. 1e), and the color returned to whitish gradually at the end of ash emission (Fig. 1f). The ash emission sometimes included scoriae without notable explosions. Some scoriae fall close to the vent, as shown in the inset of Fig. 1f. As described above, the ash emission sometimes started without notable explosions (Yokoo and Miyabuchi (2015), and personal communication with A. Yokoo). In contrast to Stromboli Volcano, it was difficult to find regularities in the ash emission and scoria ejection. We could not define the frequency of ash emission or scoria explosion quantitatively.

After May 2015, the hot water slowly recovered in the 1st crater, the eruption style changed to phreatomagmatic or phreatic eruptions, and the eruption ended in October 2016 (e.g., Miyabuchi et al. 2018).

## Samples

We collected high-porosity scoriae and ash samples at the Nakadake 3rd crater (Fig. 1c), located south of the erupting 1st crater. We also collected scoriae from the western crater rim of the Nakadake 1st crater, where the scoriae have a flattened shape (Fig. 2c, d). Sampling was conducted on March 16–17, 2015; since this period was near the end of the ash emission and Strombolian episode during 2014–2015 (e.g., Marumoto et al. 2017; Miyabuchi et al. 2018; Yokoo and Miyabuchi 2015), our samples can include the ejecta from vigorous activities during November–December 2014. We use the term porosity as the volume fraction of vesicles (in solid) and bubbles (in liquid) relative to the whole volume of a scoria, which is the same as the vesicularity for a sample without fracture and or secondary spaces formed due to crystallization.

### Scoria sample

In the thick black ash deposit at the 3rd crater, high-porosity scoriae were buried approximately 0.2 m below the surface of the deposit. We could not identify which events generated these deposits. The high-porosity

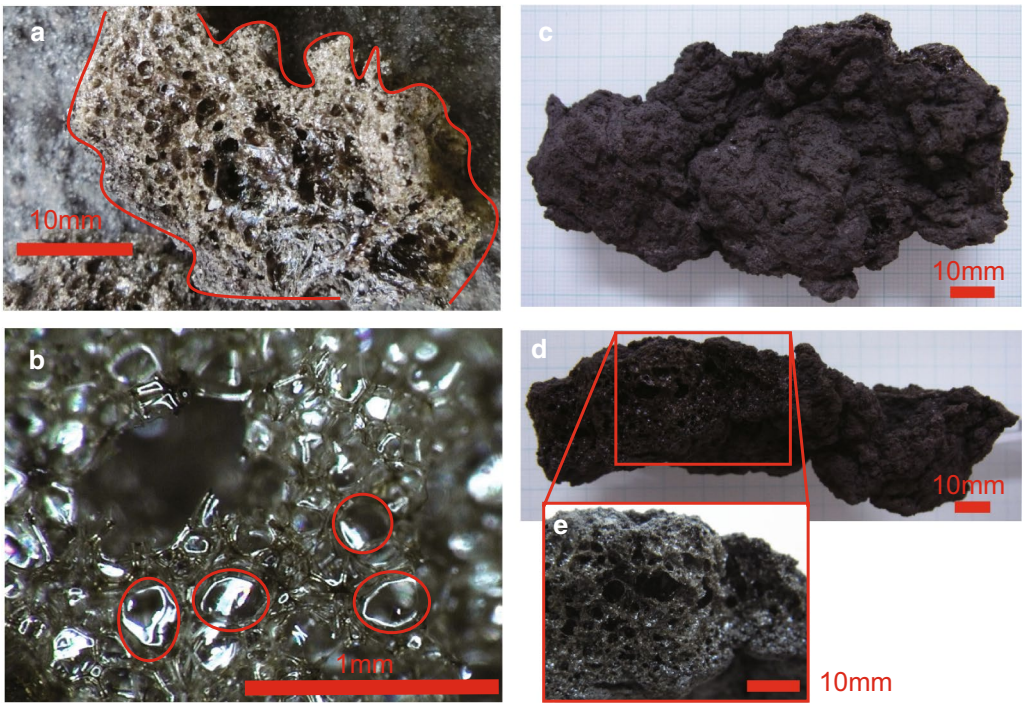


**Fig. 2** Photographs of scoriae and their magnified views. **a** A high-porosity scoria found at the 3rd crater (Fig. 1c). The red curve outlines the scoria. **b** Magnified view of the high-porosity scoria. Red circles indicate the typical vesicle sizes. **c**–**e** A flattened scoria found at the western rim of the 1st crater observed from the top (**c**) and side (**d**), and the **e** broken-out section denoted by the red rectangle in (**d**). The aspect ratio (thickness/width) of this flattened scoria is 1/3

scoriae have a yellowish color (Fig. 2a, b). The high porosity and yellowish color are similar to the golden pumices described at Kilauea, Hawaii, and Villarrica, Chile (Gurioli et al. 2008; Sharp et al. 1987). The magnified view shows ordered vesicles with a honeycomb structure (Fig. 2b).

The scoriae found at the western crater rim were not buried in the ash layer and are characterized by large ranges of the porosity and vesicle size. Figure 2e shows magnified views of the cross section of the scoria. Apparently, the vesicularity decreases from the inside of the sample toward the edge. The vesicle radii are also smaller from the inner of the sample toward the edge. These structures suggest that the scoriae that landed at the crater rim were sufficiently hot to be flattened by gravity (Yokoo and Miyabuchi 2015), and the bubbles at the surface of the scoriae could shrink.

We measured the porosity of 18 fragments of scoriae in total, consisting of six fragments from three regions: the surface of the scoriae, the internal high-porosity region, and the regions including both the inside and surface. Here, it was difficult to excavate the fragile scoriae without deficiency. The large scoriae found on the road usually fractured. We thus could not obtain the porosity and size of whole clasts. For the same reason, the number of analyzed samples is limited. We measured the mass ($m_s$) and volume of the scoriae coated by a paraffin film and immersed within water ($V_t$) (e.g., Shea et al. 2010). The density of the solid part of the scoriae, $\rho_s = 2720\,\mathrm{kg\,m^{-3}}$, was obtained by weighing and measuring the volume of the grounded scoriae using a pycnometer.

The measured porosities of the scoriae ($\phi_b = 1 - (m_s/\rho_s)/V_t$) are in a range of 0.7–0.94. The average porosities around the outer edge, inside, and a mixture of both are 0.76, 0.88, and 0.82, respectively. Here, the classification of the locations, outer edge, inside, and the mixture of both, is not strict. Again, the high-porosity scoriae are fragile, and it is difficult to cut them at an ideal location. This range is close to that reported for high-porosity reticulite, 0.75–0.98 (Mangan and Cashman 1996), formed in the lava fountain in Kilauea.

We estimated the vesicle-free crystallinity (relative to the melt volume) as $< 0.47$, which is similar to that reported for Stromboli Volcano, 0.35–0.6 (Gurioli et al. 2014). We calculated the crystallinity by measuring the areal fraction of crystals in the thin section image of the molten sample (Fig. 3b) described in the next section. This is because the high porosity of the scoria made it difficult to evaluate the melt area from the thin section image of the scoria (Fig. 3a). In the molten sample, crystals sink, and the thin section is created in the crystal-rich region. Thus, the crystallinity of 0.47 is the maximum estimate.

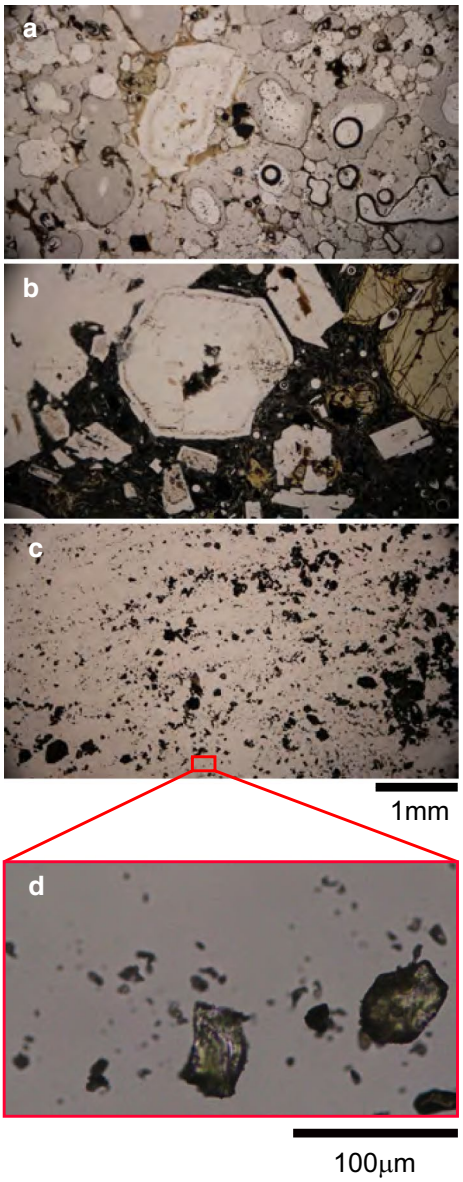


**Fig. 3** Thin section images of a scoria and ash. **a** Open nicol image of a typical high-porosity scoria (Fig. 2a). **b** Open nicol image of the molten scoria shown in Fig. 4f. **c** Ash observed by a microscope showing the existence of fine ash $< 63$ μm. **d** Magnified view of (**c**)

## Ash sample

We collected ash sediments at the 3rd crater. The reported characteristics of ash are divided into two groups, which are brownish glass and black ash (Geological Survey of Japan and Kyoto University 2015; Toma

et al. 2017). Some glassy ash is characterized by vesicles and has elongated shapes (Geological Survey of Japan and Kyoto University 2015).

Figure 3c, d shows photographs of ash spread on the plate homogeneously to the best of our ability and shows that both coarse $< 1$ mm and fine $< 63\,\mu$m ashes exist. Fine ash may be rare in basaltic eruptions but is observed in El Chichon (e.g., Cashman and Rust 2016). Our sample could contain small particles generated by sedimentation processes (e.g., Buckland et al. 2018; Dufek and Manga 2008; Kueppers et al. 2012). However, fine ash was also reported by Geological Survey of Japan and Kyoto University (2015). During November 26–December 4, 2014, Geological Survey of Japan analyzed the ash directly sampled without landing at 2.2 km and 1.2 km from the vent and reported that 25–60 wt.% of ash particles were smaller than 63 μm. Black ash was 60–70%, brown ash was 10%, and altered clasts were 10%. For December 3–16, 2014, the fraction of fine ash was reduced to 1–25 wt.% and the fraction of brown ash increased to 50–60%. In January 2015, the fraction of brown ash was approximately $> 40$ %; thus, we consider that our sample includes the deposits from these activities.

We sieved ash with meshes of 53 μm and 1 mm in a 35-mm-diameter dish. In order to conduct a shear deformation experiment with a small thickness ($\leq 6$ mm), we used a sieve with finer mesh size (53 μm) than the threshold for fine ash ($\leq 63\,\mu$m).

## Experiments on shrinkage due to heating

In this section, we heat the scoria samples and measure their shrinkage to estimate the temperature when the scoriae erupted. The erupted scoriae found on the west side of the crater showed a flattened shape, which might have originated from gravitational deformation (Fig. 2c, d). For such deformation, the scoriae had to be erupted at a high temperature to make their viscosity low. In addition, the flattened scoriae have an outer edge with small vesicles. If the surrounding melt had a sufficiently low viscosity, the vesicles in the scoriae close to the outer edge might experience shrinkage.

The surface tension-induced shrinkage of bubbles in magma has been reported for andesitic and rhyodacite pumice (Kennedy et al. 2016; Otsuki et al. 2015). When hot pumice having interconnected bubbles is exposed to constant pressure at high-temperature conditions, the bubbles can shrink owing to the surface tension effect. This may be the mechanism that generates the low-porosity region with small vesicles around the outer edges of scoriae. To evaluate the temperature range for shrinkage, we heated the scoria samples and measured their volume change.

### Heating procedure

We placed the scoria samples into a preheated muffle furnace at the predetermined temperature. By inserting the sample, the internal temperature of the furnace drops. Irrespective of this temperature drop, we measured the heating time after we placed the sample in the furnace. We used the scoria samples without arranging their shape because they are difficult to reshape. Thus, the initial shapes of the scoriae are irregular. We measured the initial and final volumes of the scoriae.

### Measured shrinkage

Figure 4 shows the volume change after heating. Here, the temperatures marked in the figure indicate the furnace temperature at the end of heating. When we placed the samples in the furnace, the internal temperature of the furnace drops. It takes a long time to recover the internal temperature; consequently, short heating experiments cannot reach a high temperature.

For the short heating time (5 min) at a temperature of 965 °C, the volume change of the scoria is limited. For the longer heating time (15 min) at 1055 °C, the scoria shrinks and turns into a reddish color because of oxidation. When the scoria is kept at 1150 °C for 1 h, bubbles perfectly segregate from the melt.

Figure 5 summarizes the heating experiments. We heated scoria samples in a furnace with various initial porosities (0.63–0.92) and volumes (0.5–2.7 ml) and measured the volume change. We conducted more experiments at a shorter heating time <500 s (lower temperature) than those at a longer heating time (higher temperature). This is because the volume change at a low temperature was not obvious, and we needed to check the repeatability (Fig. 4).

Figure 5a shows that longer heating at a higher temperature makes the scoriae shrink. Comparing the same heat duration (30 s) experiments, scoriae having a smaller volume as an initial condition effectively shrink. This is because, in order to decrease the volume, the gas inside the scoriae has to escape to the atmosphere by permeable flow. The bubbles close to the scoria surface may connect to the atmosphere, but the internal bubbles may not. Larger scoriae can include disconnected bubbles whose volume is not changed by heating.

As the volume decreases, the porosity of the scoriae also decreases (Fig. 5b). When the furnace temperature is 1055 °C, the minimum porosity of the scoriae becomes approximately 0.6, close to the random packing of spheres (e.g., Namiki and Tanaka 2017, and the references therein). Here, a change in the connectivity may occur as a governing mechanism of the final porosity. However, we could not check the evolution of the connectivity because of the difficulty of the shape forming

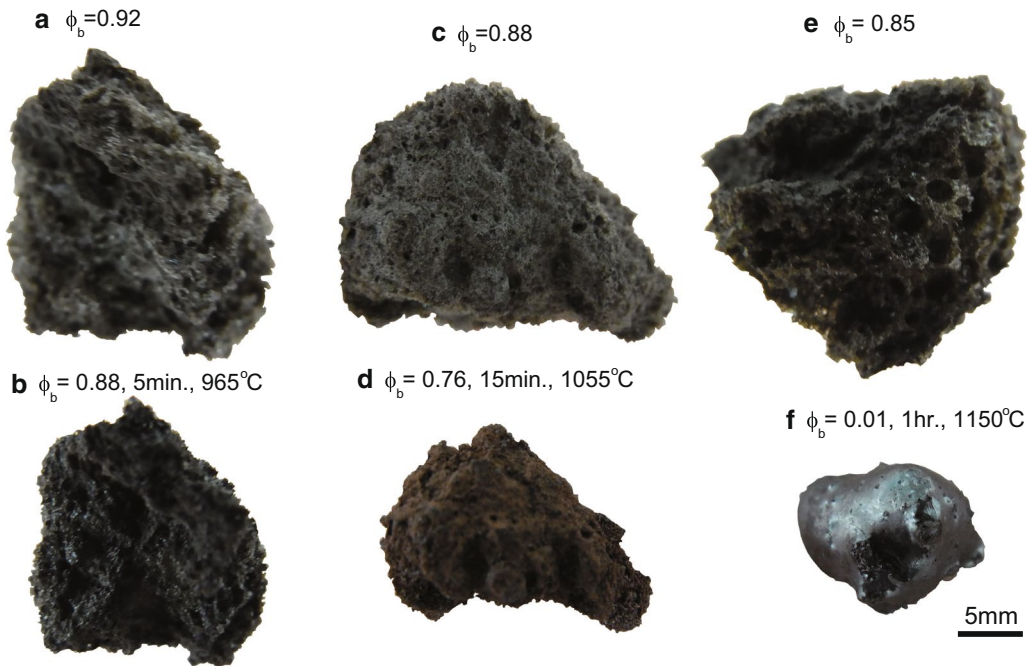


**Fig. 4** Photographs of scoriae shrunk by heating. **a**, **c**, **e** and **b**, **d**, **f** show the photographs and porosities of scoriae before and after heating, respectively. Initially, the muffle furnace is kept at 1150 °C. When we open the furnace to place the samples inside, the internal temperature drops. We include this recovery time in the heating time

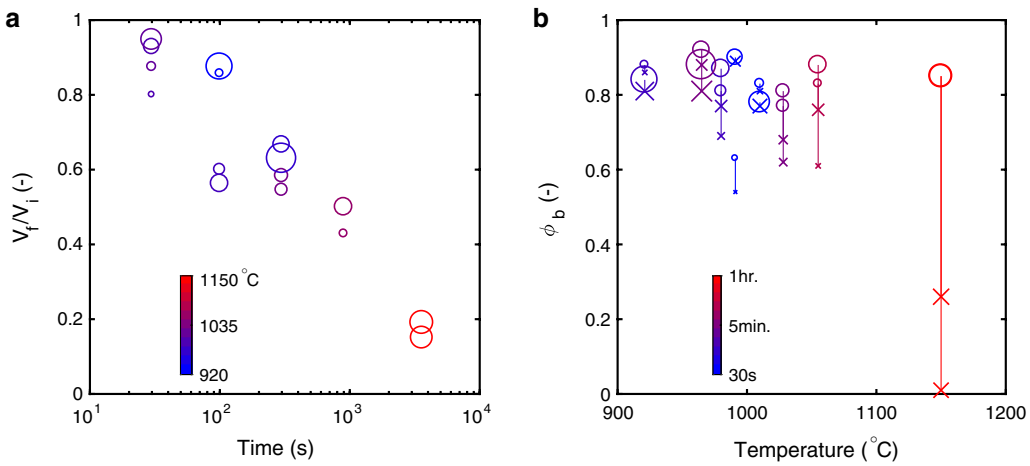


**Fig. 5** Measured shrinkage due to heating. **a** The volume ratio of scoriae after ($V_f$) to before ($V_i$) heating as a function of the heating duration. The symbol color indicates the furnace temperature at the end of heating, and the symbol size indicates the initial volume of the scoria. **b** The porosity change due to heating. Each set of circles and crosses connected by a line indicates the porosity change of a scoria before and after heating, respectively, as a function of the furnace temperature at the end of heating. The symbol color indicates the heating duration, and the symbol size indicates the initial volume of the scoria

of fragile scoriae. When the furnace temperature is sufficiently high, 1055 °C, the scoriae melt and become sufficiently less viscous; therefor bubbles segregate by buoyancy rather than permeable flow. As a result, their porosity becomes lower than 0.4.

#### Estimated timescale of shrinkage and eruptive temperature

Here, the timescale of the relaxation of bubbles with a radius $r_b$ induced by the surface tension $\xi$ surrounded by a melt with a viscosity of $\eta_m$ is approximated by

$$\tau = \frac{\eta_m r_b}{\xi}. \quad (1)$$

The typical vesicle size shown in Fig. 2b is $r_b < 1$ mm, the surface tension of the melt is on the order of $\xi \sim 0.1\,N\,m^{-1}$ (e.g., Walker and Mullins 1981), and the viscosity of water-free basaltic andesite is $\eta_m \sim 10^3$ Pa s at 1000 °C (Giordano et al. 2008). The timescale for bubble relaxation is < 10 s, which is sufficiently shorter than the duration of heating in Fig. 5a. We thus consider that the bubbles are relaxed at the achieved temperature, and the maximum achieved temperature, rather than the heating duration, determines the occurrence of shrinkage. Here, crystals are densely located at the plateau border and rarely in the vesicle walls (Fig. 3a). Because the surface tension-induced shrinkage is the process of the bubble wall thickening, the crystals at plateau borders do not significantly affect the shrinkage.

It is known that a high crystallinity enhances the connectivity of bubbles and permeable outgassing from the inside bubbles (Lindoo et al. 2017; Moitra et al. 2013), which in turn affects the eruption styles. Here, the crystallinity of scoriae from Aso eruption is high and <0.47, but the porosity is also high and >0.7. Again, the crystals densely locate at the plateau borders and each group does not contact (Fig. 3a). We thus infer that the crystals do not make a frame to enhance the outgassing from the magma in the conduit so that the magma in the conduit can achieve a high porosity. Once the high-porosity magma erupts out as a scoria, bubbles close to surface of the scoria shrink by surface tension to create a low-porosity outer edge (Fig. 2).

Our heating experiments show that the shrinkage of scoriae occurs at a temperature 950 °C, while the bubbles in the scoria at a temperature of 1150 °C segregate from the melt. We thus consider that the eruptive temperature of the scoriae is within the range of $950 < T < 1150$ °C. This estimate is consistent with the pre-eruptive temperature of 1000°–1100° estimated by standard geothermometry (personal communication with Saito).

## Shear deformation experiments

The magma foam in the conduit may fracture to generate ash. If the ash behaves as a continuous material, the stress beneath the ash column is approximated by the lithostatic pressure. On the other hand, if the ash behaves as a granular material, the maximum stress beneath the ash column scales with the width of the conduit, irrespective of its vertical length (e.g., Duran 1999; Janssen 1895; Roberts et al. 1883). For example, when the height of a granular column in a silo increases little by little, the stress at the bottom of the silo saturates around a thickness close to the width of the silo, known as Janssen effect (e.g., Duran 1999; Janssen 1895; Roberts et al. 1883). The loading of the granular material is sustained by the force chain connected to the wall.

The strength of the bubbly magma regulating the ash formation depends on the structures of the pores (Al-Harthi et al. 1999; Bubeck et al. 2017; Heap et al. 2014; Zhu et al. 2010). The high porosity of Aso scoriae may dramatically reduce the fracture strength. The frictional strength of ash has been measured, and both rate weakening and rate strengthening have been reported (e.g., Kennedy and Russell 2012; Lavallee et al. 2014; Moore et al. 2008). Basically, rate strengthening is observed in a faster deformation regime than rate weakening. In this section, we provide the fracturing conditions of scoriae and the frictional strength of ash in the conduit at a high temperature (< 500 °C) and low normal stress (<100 kPa). We also provide the conditions for sintering which changes the mobility of ash particles (Vasseur et al. 2013).

#### Methods of shear deformation

We conduct shear deformation experiments by using a rheometer (Anton Paar MCR102). The samples are sandwiched between two parallel plates made of Inconel and placed inside a temperature-controlled oven, the same method used in Gonnermann et al. (2017) and Namiki and Tanaka (2017). The maximum temperature achieved by this oven is 1000 °C. We heat the oven to the desired temperature $T$; wait >15 min at $T$, which is sufficiently longer than the thermal diffusion time; and then deform the sample under a certain normal stress. Here, we conducted our experiments at a temperature lower than the upper limit of our apparatus, < 1000 °C. This temperature range is lower than the previously estimated eruptive temperature, $950 < T < 1150°$, and may be consistent with the temperature at the uppermost part of the magma column in the conduit during the quiescent time.

From the deflection angle $\theta$, angular velocity $\dot{\theta}$, and torque required to deform the sample $\Gamma$, we obtain the strain $\gamma$, strain rate $\dot{\gamma}$, and shear stress $\sigma_\tau$:

$$\gamma = \frac{2R\theta}{3h}, \tag{2}$$

$$\dot{\gamma} = \frac{2R\dot{\theta}}{3h}, \tag{3}$$

$$\sigma_\tau = \frac{4\Gamma}{3\pi R^3}, \tag{4}$$

where $R$ and $h$ are the sample radius and thickness, respectively. In this measurement, the disk-shaped sample reduces the stress anomaly, resulting in more precise measurements. However, the high-porosity and fragile scoriae cannot be trimmed into a disk shape. We thus used irregular-shaped sample plates by grounding the upper and lower surfaces of the relatively thin scoriae to obtain a constant thickness $h$ (Fig. 6). The average radius of a sample is calculated from its surface area, $R = (S/\pi)^{1/2}$, and the error caused by this approximation is less than 20%.

Our rheometer can control the normal force $F_\mathrm{N}$, and the normal stress is calculated by

$$\sigma_\mathrm{N} = F_\mathrm{N}/S. \tag{5}$$

We varied the normal force within the range lower than the upper limit of our apparatus of $< 25$ N. The cross-sectional area of the scoria samples also varies the normal stress within the range of $\sigma_\mathrm{N} < 90$ kPa. This stress range is consistent with the lithostatic pressure at depths shallower than 3 m.

The ratio of the shear stress to the normal stress is known as the friction coefficient

$$\mu = \sigma_\tau/\sigma_\mathrm{N}. \tag{6}$$

Two kinds of shear deformation are used in these measurements: unidirectional steady shear and oscillatory shear. Steady shear generates a large strain so that the accumulated stress may be able to cause fracturing. As steady shear, we imposed a shear rate $< 0.1\ \mathrm{s}^{-1}$ within the possible torque range of our apparatus of $< 200$ mN m, which consists with the ascent of magma at $< 0.1\ \mathrm{m\ s}^{-1}$ in a conduit with a width of 1 m.

In the oscillatory measurements, a strain $\gamma_0 e^{i\omega t}$ is imposed, and the stress required for deformation, $\sigma_\tau = |G^*|\gamma_0 e^{i(\omega t+\delta)}$, is measured, where $\omega$ is the angular frequency of oscillatory deformation, $\gamma_0$ is the strain amplitude, $|G^*|$ is the complex shear modulus, and $t$ is the time. The phase difference $\delta$ between the imposed strain and the measured stress is related to the ratio of the energy stored by elastic deformation to the loss of energy

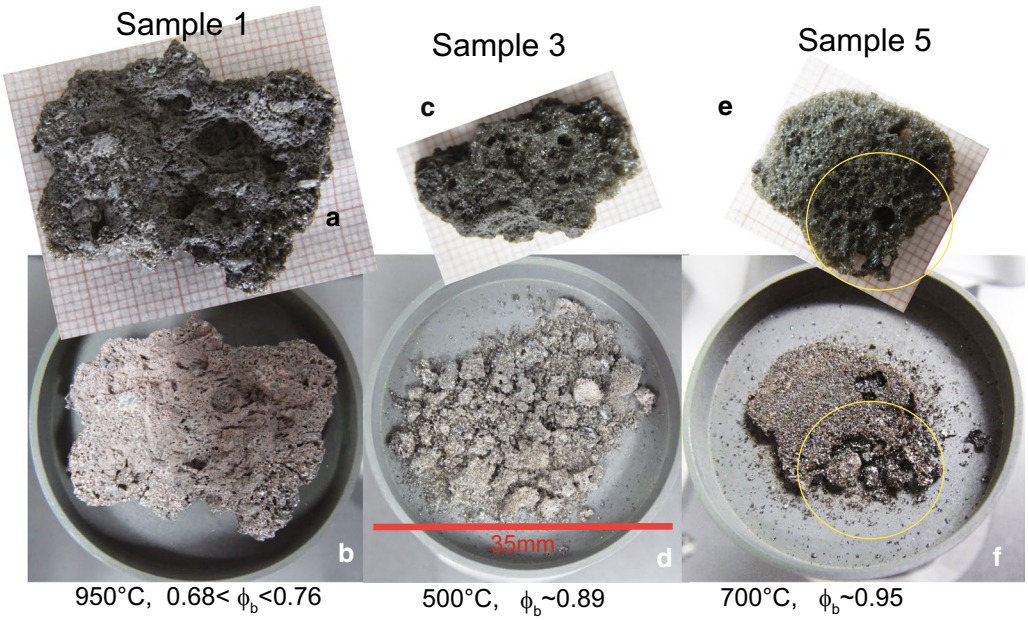


**Fig. 6** Pictures of scoriae fractured by shear deformation. Pairs **a**, **b**, **c**, **d**, and **e**, **f** show photographs of Samples 1, 3, and 5 in Table 1 before and after shear deformation, respectively; **a** shows the scoria before Run 1, and **b** is after Run 3. **b** Shows shrinkage. **d** Shows fracturing into several blocks with various sizes. **f** Shows partial fracturing. High-porosity parts denoted by the yellow circles fracture and generate small particles, but other parts shrink

**Table 1 Details of the scoria deformation experiments. $\phi_{b(Initial)}$ and $\phi_{b(Deformed)}$ are the initial and final values of the bubble fraction in the scoria, respectively**

| Sample | Run | Temperature (°C) | Thickness (mm) | $\phi_{b(Initial)}$ | $\phi_{b(Deformed)}$ | S ($mm^2$) | $\sigma_N$ (kPa) | Results |
|---|---|---|---|---|---|---|---|---|
| 1 | 1 | 950 | 9.7 | 0.76 | – | 670 | 1.5 | Shrink |
| 1 | 2 | 950 | 6.4 | – | 0.74 | 690 | 7.3 | Shrink |
| 1 | 3 | 950 | 6.3 | 0.74 | 0.68 | 680 | 37 | Shrink |
| 2 | 4 | 950 | 5.6 | 0.83 | 0.66 | 335 | 75 | Shrink |
| 3 | 5 | 500 | 5.8 | 0.89 | – | 310 | 82 | Fractured |
| 4 | 6 | 500 | 6.4 | 0.72 | – | 650 | 38 | Fractured |
| 5 | 7 | 700 | 4.3 | 0.95 | – | 300 | 83 | Partially fractured |

*S* is the surface area of the scoria, and $\sigma_N$ is normal stress to be imposed

by dissipation (Namiki and Tanaka 2017), known as the inverse of the attenuation:

$$Q = \frac{1}{\tan\delta}. \tag{7}$$

For $Q > 1$, the sample behaves as an elastic material, while for $Q < 1$, the energy imposed on the sample dissipates. We discuss the importance of $Q$ on sample fracturing and sintering. In this paper, we varied $\omega$ and $\gamma_0$ independently.

## Deformation of a scoria

### *Steady shear deformation of scoriae*

Table 1 and Fig. 6 present the samples used in these series of measurements. We used five samples. Sample 1, with an initial porosity, $\phi_{b(Initial)} = 0.76$, is deformed at 950 °C. Under three different normal stresses, $\sigma_N = 1.5, 7.3$, or 37 kPa, we conducted oscillatory measurements with varying values of $\omega$ and $\gamma_0$ and then imposed a steady shear deformation denoted as Runs 1–3 in Table 1. After each measurement, we observed the sample at room temperature and found no fracturing. Sample 2 with a higher initial porosity of 0.83 was deformed at 950 °C and has a crack.

On the other hand, Sample 3 with $\phi = 0.89$ deformed at $T = 500\,°C$ under $\sigma_N = 82$ kPa fractures into several blocks with a size $< 5$ mm and fine particles. The fractured sample spreads into a larger area (Fig. 6c, d). In this experiment, we first imposed a steady shear deformation, confirmed the fracturing by looking at the cooled sample, heated the sample again, and conducted oscillatory measurements with varying $\omega$. Sample 5 with $\phi = 0.95$ deformed at $T = 700\,°C$ under $\sigma_N = 83$ kPa partly fractures. Figure 6e and f shows that the region with large bubbles fractures. Comparing Runs 5 and 7 (Table 1), the imposed normal stress is approximately the same, but the initial porosity $\phi_{b(Initial)}$ is higher in Run 7 than that in Run 5, suggesting that the higher temperature in Run 7 disrupts the fracturing.

Figure 7a shows the time evolution of the normal and shear stresses of Sample 3 in Fig. 6c and d for a shear rate of $\dot{\gamma} = 0.006\,s^{-1}$ for 0–300 s and $\dot{\gamma} = 0.03\,s^{-1}$ for 300–400 s. The normal stress increases with time until

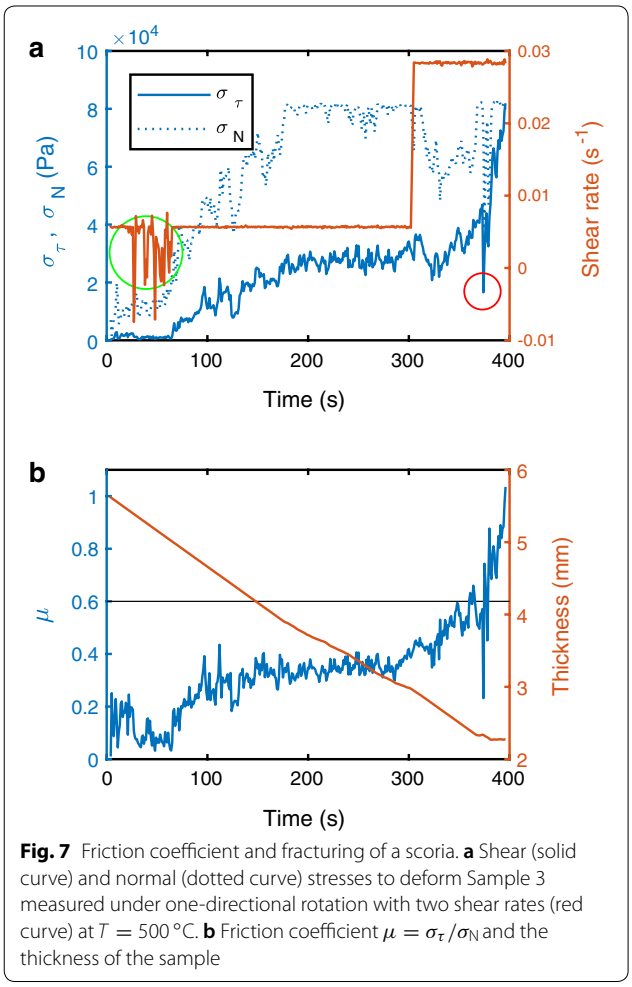


**Fig. 7** Friction coefficient and fracturing of a scoria. **a** Shear (solid curve) and normal (dotted curve) stresses to deform Sample 3 measured under one-directional rotation with two shear rates (red curve) at $T = 500\,°C$. **b** Friction coefficient $\mu = \sigma_\tau/\sigma_N$ and the thickness of the sample

reaching the desired value of $\sigma_N = 82$ kPa. Both the shear stress and friction coefficient increase with the normal stress and reach steady state (Fig. 7b). Given the undeformed bubbles in the scoriae observed in Fig. 6, we consider that the measured stress originates from the frictional force between the scoria and the Inconel plate rather than from the viscous deformation of the scoriae, as has been reported for rhyolite (e.g., Okumura et al. 2015).

When the imposed shear rate increases at 300 s, the normal and shear stresses temporarily decrease and then increase. However, the friction coefficient continuously increases, suggesting that the friction coefficient increases with the shear velocity, known as rate strengthening (e.g., Kennedy and Russell 2012; Moore et al. 2008). Here, we consider that the increases in the shear stress and friction coefficient after 300 s originate from the change in the packing of the fractured clasts. During shearing, the sample thickness is decreasing. This might spread the sample to increase its surface area and the torque required for deformation. In Fig. 7, we assume that the sample area is constant so that if the real contact area increases, the apparent shear stress and friction coefficient increase. However, for 100–300 s, the friction coefficient is approximately constant irrespective of the decreasing sample thickness. In addition, the shear stress decreases once after 300 s, but the friction coefficient continuously increases. We thus consider that the rapid shear rate after 300 s makes the fractured clasts denser and increases the friction coefficient. After 400 s, the required torque reached the upper limit of our rheometer; thus, we could not obtain later data.

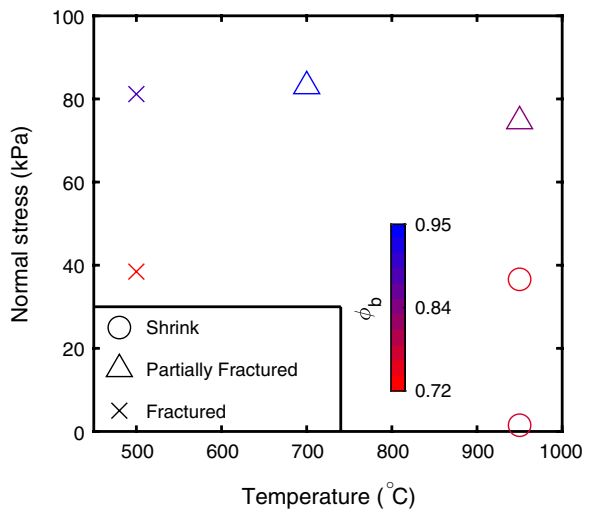


**Fig. 8** Regime diagram of fracturing. Symbol shapes indicate the occurrence of fracturing, and the symbol color indicates the initial porosity, as denoted by the color bar

In Fig. 7, it is unclear exactly when the scoria fractures. One possible time may be around 50 s, as denoted by the green circle. The shear rate deviates from the desired value, suggesting that an unexpected fluctuation in the shear stress occurs upon fracture. This hypothesis is consistent with the decrease in the observed thickness, indicating that the fractured sample spreads with time, becoming thinner. Here, if sudden fracturing occurs, the sample thickness may be decreased stepwise. We infer that fracturing of the bubble walls continuously ensues, and our apparatus does not have a sufficient time resolution to adjust the sudden decrease in the thickness. Another significant signal is indicated by the red circle. After this time, there is no longer any decrease in the sample thickness. We infer that the space between the upper and lower plates becomes thin, the same as the size of the hard crystal grains in the scoria. If this is true, fracturing occurs at a low normal force of $\sim 10^4$ Pa and a shear stress $< 10^4$ Pa, indicating that a high-porosity scoria easily fractures at a low temperature.

Figure 8 summarizes the occurrence of fracturing and shows that a low temperature and high porosity promote fracturing at certain normal stresses. We determined the occurrence of fracturing by visual observation of the deformed scoriae at room temperature. The most important result from these measurements is that the fracturing of high-porosity scoriae occurs at low normal and shear stresses with an order of magnitude of $10^4$ Pa. For an intact basalt at room temperature and a negligible confining pressure, the tensile strength is −14 MPa, the compressive strength is 262 MPa, and the fracture toughness is 1–3 MPa $m^{1/2}$ (Schultz 1993). The compressive strength of basalts with pores can decrease to as low as 10 MPa for $\phi_b < 0.7$ (Al-Harthi et al. 1999; Bubeck et al. 2017).

### *Oscillatory deformation of scoriae*

To confirm the importance of the temperature on fracturing, we next show the results from oscillatory measurements, from which we can evaluate whether the sample behaves as solid-like elastic materials or dissipative viscous fluids.

Figure 9a and b shows the oscillatory measurements of the friction coefficient, $\mu = \sigma_\tau/\sigma_N$, and $Q$ as a function of $\omega$. Circles indicate the measurements of Sample 1 around 950 °C with various normal stresses, as shown in the legend. Three measurements of $\mu$ overlap, irrespective of the difference in the normal stress. Under viscous deformation, the shear stress does not depend on the normal stress; thus, the friction coefficient $\mu$ should vary with the normal stress. On the other hand, under frictional

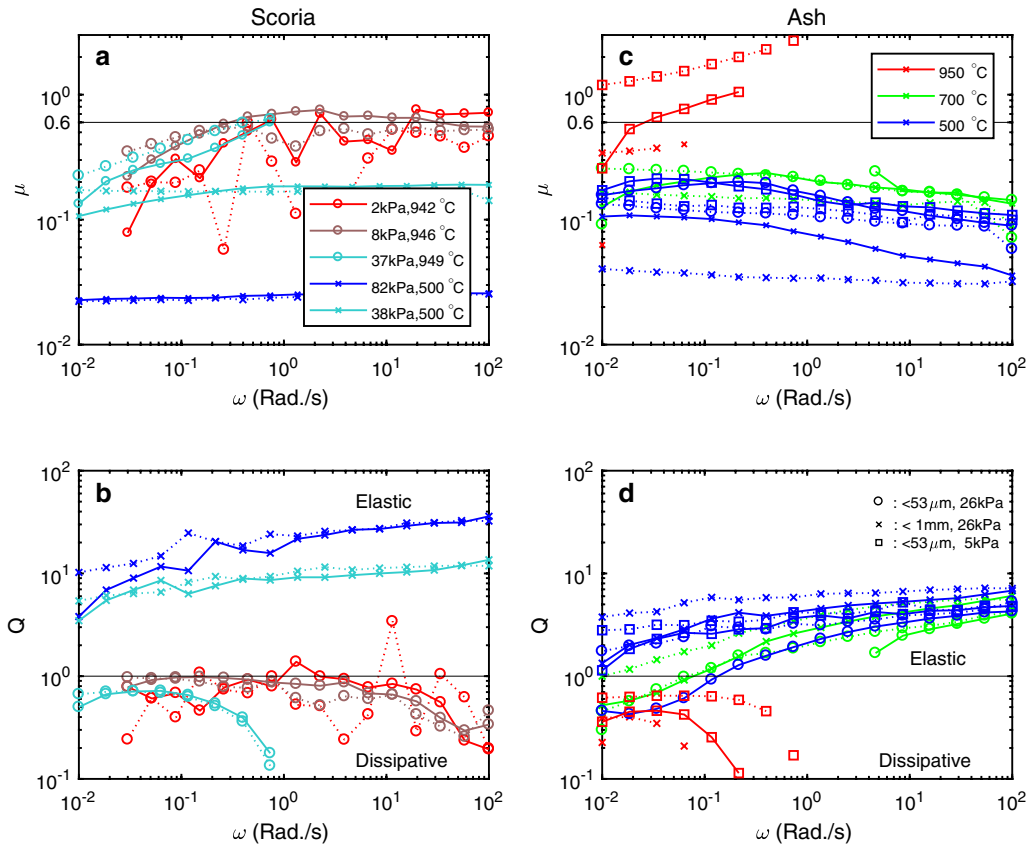


**Fig. 9** Oscillatory measurements of scoriae (**a**, **b**) and ash (**c**, **d**). **a** The friction coefficient calculated by the ratio of the shear to normal stresses, $\mu = \sigma_\tau / \sigma_N$, obtained by oscillatory measurements as a function of the angular frequency $\omega$. The color of the curves indicates the imposed normal stress as shown in the legend. Crosses and circles indicate the fractured and unfractured samples, respectively. Solid and dotted curves indicate the increasing and decreasing angular frequency $\omega$, respectively. **b** $Q$ (inverse of the attenuation) calculated by the phase difference between the imposed strain and the measured stress. When the energy dissipation exceeds the elastic energy, $Q < 1$, and vice versa. Symbols and colors are the same as those in (**a**). **c**, **d** Same as (**a**, **b**) but for ash. The color of curves indicates the temperature, and symbols indicate the combinations of the size of the ash particles and the normal stresses. In these measurements, we use a strain amplitude of $\gamma_0 = 10^{-3}$

deformation, the shear stress increases with the normal stress so that $\mu$ does not depend on the normal stress. We thus consider that the deformation mechanism is basically friction, even at a high temperature of 950 °C.

The measured friction coefficient for a low normal stress (2 kPa, red curve) is scattered. This may be due to the irregular shape of Sample 1. For a low normal force, only few asperities on the sample contact the upper and lower plates; therefore, a subtle change in the number of asperities in contact causes a fluctuation in the measured values. As the normal stress increases, the number of asperities in contact increases, and the measured data become smooth.

Under rapid deformation, $\omega > 1\,\mathrm{Rad.s}^{-1}$, the friction coefficient becomes $\mu \sim 0.6$. At slower deformation, $\omega < 1\,\mathrm{Rad.s}^{-1}$, the friction coefficient is lower, suggesting rate strengthening.

The low-temperature measurements (500 °C) shown by the crosses in Fig. 9a indicate a much lower friction coefficient than that measured at a high temperature (950 °C). The measured friction coefficient is also lower than that measured under steady shear at the same temperature (Fig. 7). The oscillatory measurements were taken after steady shear deformation. When we conducted the oscillatory measurements at 500 °C, most of fragile particles already became powder-like ash, and only the hard grains come into direct contact with the upper and lower plates (Fig. 6d), so that the apparent friction coefficient becomes low. We also measured the strain amplitude dependence of the friction coefficient $\mu$ with a fixed $\omega = 6.2\,\mathrm{Rad.\,s}^{-1}$. In the range of $10^{-4} < \gamma_0 < 10^{-2}$, the friction coefficient is approximately constant.

In Fig. 9b, there is a correlation between $Q$ and the occurrence of fracturing. The measurements at 950 °C indicated by the circles show that $Q < 1$, suggesting

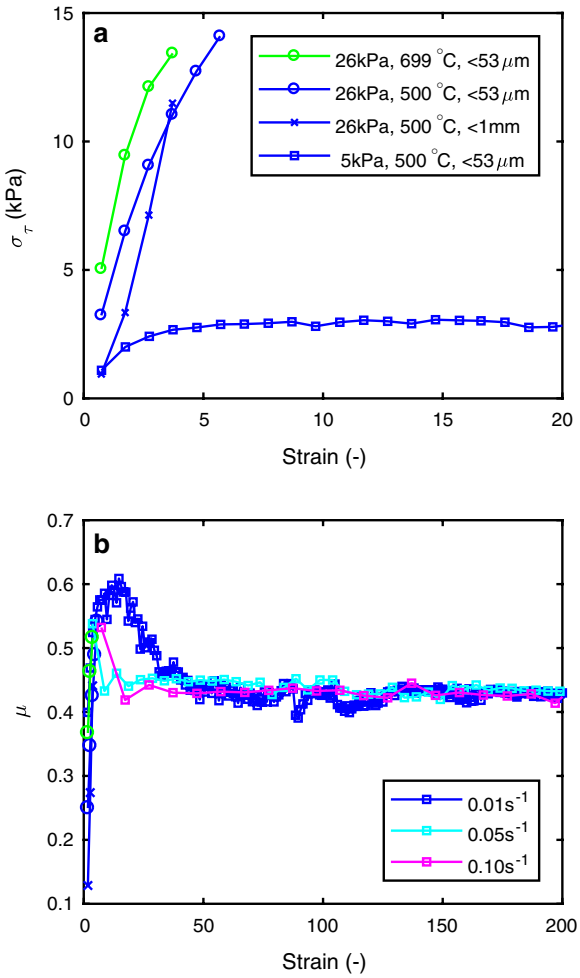


**Fig. 10** **a** Stress and **b** friction coefficient of ash measured by steady shear deformation. **a** Shear stresses measured under one-directional rotation with a shear rate of 0.01 $s^{-1}$ at various normal stresses, temperatures, and grain sizes. **b** Friction coefficient as a function of the strain and shear rate

that the imposed energy for deformation is dissipated, in which fracture does not occur. This result suggests that elastic energy has to be accumulated for fracturing.

From these measurements, we infer that ash is easily generated at a low temperature (< 700 °C). If the surrounding temperature is high and the bubbles in the magma do not have excess pressure, the bubbles shrink owing to the surface tension to reduce the porosity. The scoriae with a low porosity have thick bubble walls, which prevent fracturing to generate ash.

### Deformation of ash

Table 2 presents the list of friction measurements of the ash rheology. We deformed the ash sieved with meshes of 53 μm and 1 mm in a 35-mm-diameter dish by rotating the upper plate at a certain temperature and normal stress. The measurements are taken in the order of frequency-varying oscillation and then steady shear deformation. As with the measurements of scoriae, we could not obtain some data because of the torque limitation.

The ash layer with small particles (< 53 μm) at 950 °C is sintered to generate the ash plate. The ashes at a low temperature (≤ 700 °C) and high temperature (950 °C) with large particles (53–100 μm) do not sinter.

Ash is a granular material having a porosity; hence, the compacted ash layer becomes thinner during measurement at a certain normal stress. The maximum porosity measured by pouring the ash sample into a measuring cylinder ($\phi_{b(Random)}$) is larger than the porosity after the measurement calculated from the thickness of the ash layer ($\phi_{b(Compacted)}$), i.e., $\phi_{b(Random)} > \phi_{b(Compacted)}$. The mass of the collected ash sample after the measurement is more than 99% of the initial value, indicating that the loss of the sample is negligible.

#### *Steady shear deformation of ash*

Figure 10a plots the stress evolution during steady shear deformation. In most of the steady shear deformation, the required torque exceeds the upper limit of our apparatus; therefore, we plot the data before reaching the upper limit. When the imposed normal stress is low (5 kPa), the required shear stress is low, and we able to continue the measurement for a long time. In contrast, for a higher normal stress (26 kPa), the required stress soon reaches the maximum, and the plots end. The measurements at a high temperature (950 °C) are not plotted in this figure because the required torque for deformation immediately exceeds the upper limit of our apparatus.

In the first 5 seconds of Fig. 10b, the friction coefficients overlap, which correspond to the measured shear stresses in Fig. 10a. For a low normal stress (5 kPa), measurement is possible for a long time, as indicated by the squares. The measured friction coefficient depends on the total strain. Initially, the friction coefficient increases to 0.6; then, it decreases to 0.4 asymptotically. During this measurement, we change the shear rate as indicated by light-blue and pink curves, which show the same friction coefficient of 0.4. We infer that the irregularly shaped ash particles aligned according to the shear deformation to reduce the frictional force.

#### *Oscillatory deformation of ash*

Figure 9c and d shows the oscillatory measurement of ash as a function of angular frequency, $\omega$. Again, the red curve is plotted only in the range of $\omega < 1$ Rad. $s^{-1}$, because of the torque limitation.

The measurements are taken by increasing and decreasing $\omega$ as shown by the solid and dotted curves, respectively. In Fig. 9c, the blue- and green-dotted curves are located below the corresponding solid curves, suggesting that the friction coefficient becomes lower with time. The alignment of irregular particles may reduce $\mu$, as shown in the steady shear deformation (Fig. 10b). In contrast, the red-dotted curve with squares is plotted above the corresponding solid curve. These curves exceed 0.6. In addition, the sample collected after the experiment sintered. We infer that the high temperature allows the ash grains to sinter, which increases the friction coefficient. Thus, the ash loses its granular characteristics.

The friction coefficient $\mu$ measured by oscillatory deformation is lower than that measured by steady shear deformation (Fig. 10b). This discrepancy may be caused by the small strain amplitude of the oscillatory measurements $\gamma_0 = 10^{-3}$. The friction coefficient measured at high axial stresses (0.5–2.5 MPa) and slow slip rate $< 0.1\,\mathrm{m\,s^{-1}}$ of $\mu = 0.7$–$0.8$ (Lavallee et al. 2014) is also higher than those shown in Fig. 9c for low-temperature measurements at $\leq 700\,^{\circ}\mathrm{C}$. The friction coefficient of ash at a low temperature ($\leq 700\,^{\circ}\mathrm{C}$) in Fig. 9c decreases with increasing angular frequency, known as rate weakening (e.g., Lavallee et al. 2014).

We note that the ratio $\mu = \sigma_\tau/\sigma_\mathrm{N}$ and $Q$ measured at 500–700 °C, shown in Fig. 9c, d, are plotted between those of the fractured and unfractured scoriae shown in Fig. 9a, b. Here, the fractured scoriae have large grains, and the ash with larger grains ($< 1$ mm) shows a lower $\mu$ and higher $Q$. These results suggest a grain-size dependence of the friction coefficient.

Comparing Fig. 9a, c may indicate the evolution of the ash in the conduit. The unbroken scoriae at 950 °C indicated by the circles in Fig. 9a show rate strengthening at low angular frequencies ( $< 1\,\mathrm{Rad.\,s^{-1}}$). As the flow rate in the conduit becomes faster, the friction between the conduit wall and the internal magma increases. In addition, the magma is eventually cooled. Finally, bubbly magma fractures. The friction coefficient of the fractured magma, containing both large and small particles, like scoriae and ash (Fig. 6d), is lower than that before fracturing but still shows rate strengthening, as indicated by the crosses in Fig. 9a. Thus, large particles (small scoriae) further break down into small particles (ash). Concurrently, the size separation of particles takes place; that is, small particles (ash) flow down in the space at the grain boundaries of large pieces (scoriae), which causes hysteresis in the friction coefficient, as shown by the blue curve with crosses in Fig. 9c, a measurement for ash with large grains at a low temperature. Once the particle size becomes uniform at each location, the frictional characteristic changes into rate weakening, as indicated by the blue and green curves in Fig. 9c, measurements for fine ash at a low temperature. If the fine ash is reheated to a high temperature, the ash sinters, and the frictional characteristics return to rate strengthening again, as indicated by the red curves in Fig. 9c.

An important correlation between the occurrence of fracturing/sintering and $Q$ appears in Fig. 9b and d. Measurements at 950 °C show that $Q < 1$, suggesting that the imposed energy is dissipated, in which fracture does not occur or sintering occurs. On the other hand, measurements at $\leq 700\,^{\circ}\mathrm{C}$ show that $Q > 1$, suggesting that the elastic energy is stored, in which fracture occurs and sintering does not occur. It has been discussed that the occurrence of fracturing is a key process controlling eruption styles (e.g., Gonnermann 2015). Recent seismic observations show the distribution of $Q$ beneath a volcano (Kumagai et al. 2014). Gathering $Q$ values under various conditions may help to assess the subsequent eruption styles (Namiki and Tanaka 2017).

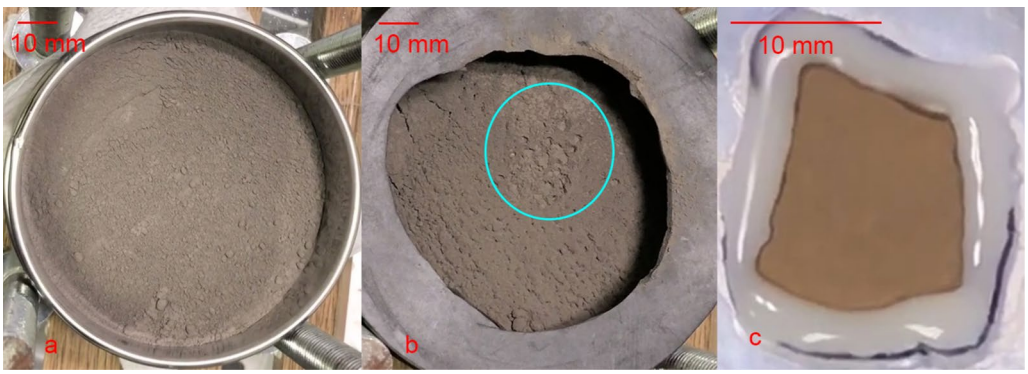


**Fig. 11** Photographs of (**a**, **b**) powder-like ash and **c** a sintered ash plate. **a** Before and **b** after the permeability measurement. The diameter of the sieve is 75 mm, and the thickness of the ash layer is 5 mm. **b** The blue circle indicates the pipe-like structure. A rubber ring used for sealing is placed on the sieve rim. **c** The brownish ash plate is embedded in a plastic case

## Permeability measurements

In the previous section, the small-particle ash (< 53 μm) heated at 950 °C at a normal stress of 26 kPa became a sintered thin plate. This condition is consistent with the bottom of the debris layer at the uppermost part of the magma in the conduit. Sintering in the conduit should reduce the mobility of ash particles (Vasseur et al. 2013). Such sintering might occur in the conduit and could affect the gas flow.

Measurement of the permeabilities of natural and synthetic pumice/scoriae has been intensively taken to evaluate the efficiency of outgassing (Klug and Cashman 1996; Takeuchi et al. 2005). The deformation of bubbles enhances their connectivity (Okumura et al. 2009). The time-dependent interconnected structure of bubbles also enhances permeability of the bubbly liquid (Namiki and Kagoshima 2014). However, it is not understood yet how the mobility of ash particles affects the permeability. In this section, we measure the permeability of unheated powder-like ash samples and a sintered ash plate (Fig. 11). Both the sintered and powder-like ashes were collected at Nakadake 3rd crater on the south side of the vent and sieved with a 53 μm mesh.

### Methods for measuring the permeability

The permeability was determined by applying pressurized gas to the sample and measuring the volumetric flow rate (e.g., Yokoyama and Takeuchi 2009). The permeability is basically defined by Darcy's law,

$$\frac{\Delta P}{L} = \frac{\eta_g}{k} v, \tag{8}$$

where $\Delta P$ is the pressure difference over the sample length $L$, $\eta_g \sim 1.8 \times 10^{-5}$ Pa s is the dynamic viscosity of the filtering gas, and $v$ is the areal flow rate calculated by the total flow rate per cross-sectional area.

When the flow rate is high, an inertial effect reduces the gas flow rate; hence, the pressure gradient within the sample becomes proportional to the square of the flow rate, known as Forchheimer's equation (e.g., Rust and Cashman 2004),

$$\frac{\Delta P}{L} = \frac{\eta_g}{k_1} v + \frac{\rho_g}{k_2} v^2, \tag{9}$$

where $\rho_g = 1.2\,\mathrm{kg\,m^{-3}}$ is the gas density, $k_1$ is the Darcian permeability, and $k_2$ is inertial permeability.

### Permeability of powder-like ash

We measure the permeability of the unheated powder-like ash placed in a sieve with a mesh size of 20 μm and an inner diameter of 75 mm. To prevent ash from flowing into the gas tube, we placed two Kimwipes sheets at the upper and lower ends of the sieve. The sieve itself has a finite permeability. We thus measure the permeability for both the empty sieve and the sieve filled with ash (Fig. 12a). The difference in the pressures measured in these two setups as a function of the flow rate is quite small.

The sieve and ash are regarded as a series of two porous media in which the areal flow rate is the same, and each porous medium causes a pressure reduction. In Fig. 12a, the total pressure reduction ($\Delta P_a$) is indicated by the red curve, and that for the sieve is indicated by the blue curve ($\Delta P_s$). The pressure reduction caused by the ash itself is $\Delta P_a - \Delta P_s$ and is shown in Fig. 12b. As the areal flow rate

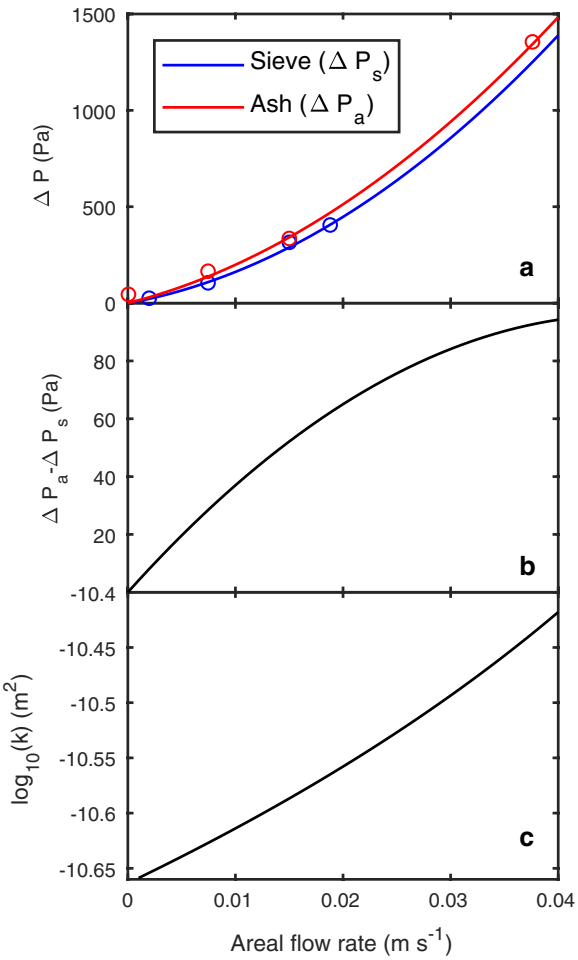


**Fig. 12** Permeability measurement of powder-like ash. **a** Required pressure difference to cause a certain areal flow rate. The blue curve shows the measurement with the empty sieve, and the red curve shows that with the ash-filled sieve. **b** The difference between the measured pressures in (**a**). **c** Calculated permeability with a linear assumption

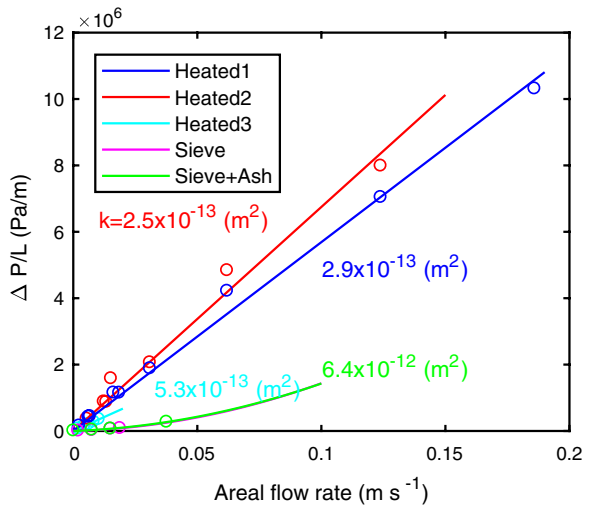


**Fig. 13** Pressure gradient as a function of the flow rate per unit area. The superimposed numbers indicate the permeabilities

increases, the required pressure increases, and its slope decreases, in contrast to Eq. (9). This may be because the powder-like ash can move according to the gas flow. If there exists a narrow pathway in which the gas flow is relatively fast, the gas flow removes obstacle ash particles, and the gas flow is further concentrated in this pathway. Such feedback increases the flow rate, and the pipe-like structures in the ash bed are maintained. Indeed, a pipe-like structure is observed after the permeability measurements, as indicated by the blue circle in Fig. 11b.

From Fig. 12b, we calculate the permeability using Eq. (8) and plot it in Fig. 12c. Upon increasing the areal flow rate, the calculated permeability increases, suggesting that the pipe-like structure develops when increasing the areal flow rate. Figure 12a suggests that the gas flow has inertia, and Eq. (9) is appropriate for calculating the permeability. However, we cannot obtain some pairs of $\Delta P$ and $v$ for the same structure. We thus use Eq. (8).

### Permeability of the ash plate

The heated ash became a sintered plate. We thus embedded the sample in a plastic frame using resin and imposed a pressure difference to cause a gas flow (Fig. 11c). Figure 13 shows a linear trend; thus, we use Eq. (8) and obtain a permeability of $2.5 \times 10^{-13}\,\mathrm{m}^2$. We measured the permeability of the same sample twice. After the first measurement, we found that most gas leaks between the sample and the resin (blue line). We then added resin between the sample and the previously located resin and measured it again (red line). During this measurement, the sample under a high pressure difference broke. We thus could no longer check the gas leakage. Accordingly, we made the sample and measured the permeability again. However, the sample had cracks during the measurement (light-blue curve). Thus, the measured permeability can still include the effect of leakage and is considered as an upper limit.

The permeability of granular material is frequently approximated by the Kozeny–Carman equation (Carman 1937) with a formulation of

$$k = \frac{r_\mathrm{s}^2}{45}\frac{\phi_\mathrm{b}^3}{(1-\phi_\mathrm{b})^2}, \tag{10}$$

where $r_\mathrm{s} < 27\,\mu\mathrm{m}$ is the radius of the ash grains sieved with a mesh size of $53\,\mu\mathrm{m}$. For $r_\mathrm{s} = 27\,\mu\mathrm{m}$ and $\phi_{\mathrm{b(Compacted)}} = 0.46$ (Table 2), we obtain $5.4 \times 10^{-12}\,\mathrm{m}^2$, which is higher than that measured for the sintered ash plate, $2.5 \times 10^{-13}\,\mathrm{m}^2$. Here, Eq. (10) is for a granular medium with a unimodal particle size distribution, and our ash includes finer particles. A small amount of finer particles drastically reduces the permeability (e.g., Koltermann and Gorelick 1995).

A more realistic empirical formulation, taking into account the various pore structures, is written in the form (Nishiyama and Yokoyama 2017)

$$k = 8.5(\phi_\mathrm{open} r_\mathrm{cr}^2)^{1.3} \tag{11}$$

**Table 2 List of friction experiments with ash. $\phi_{\mathrm{b(Ramdom)}}$ and $\phi_{\mathrm{b(Compacted)}}$ are the gas fractions in the ash before and after imposing a normal stress, respectively**

| Temperature (°C) | Sieve (μm) | Thickness (mm) | $\phi_{\mathrm{b(Random)}}$ | $\phi_{\mathrm{b(Compacted)}}$ | $\sigma_\mathrm{N}$ (kPa) | Results |
|---|---|---|---|---|---|---|
| 950 | <53 | 2.0 | 0.65 | 0.46 | 26 | Sintered |
| 950 | 53–1000 | 3.2 | 0.46 | 0.43 | 26 | Partially sintered |
| 950 | <53 | 2.3 | 0.65 | 0.54 | 5.1 | Sintered |
| 700 | < 53 | 2.0 | 0.65 | 0.47 | 26 | Powder |
| 700 | 53–1000 | 3.0 | 0.46 | 0.40 | 26 | Powder |
| 500 | <53 | 2.1 | 0.65 | 0.48 | 26 | Powder |
| 500 | 53–1000 | 2.8 | 0.46 | 0.37 | 26 | Powder |
| 500 | <53 | 2.3 | 0.65 | 0.52 | 5.1 | Powder |

The thickness is the final value of the measurement, and $\sigma_\mathrm{N}$ is the desired normal stress to be imposed

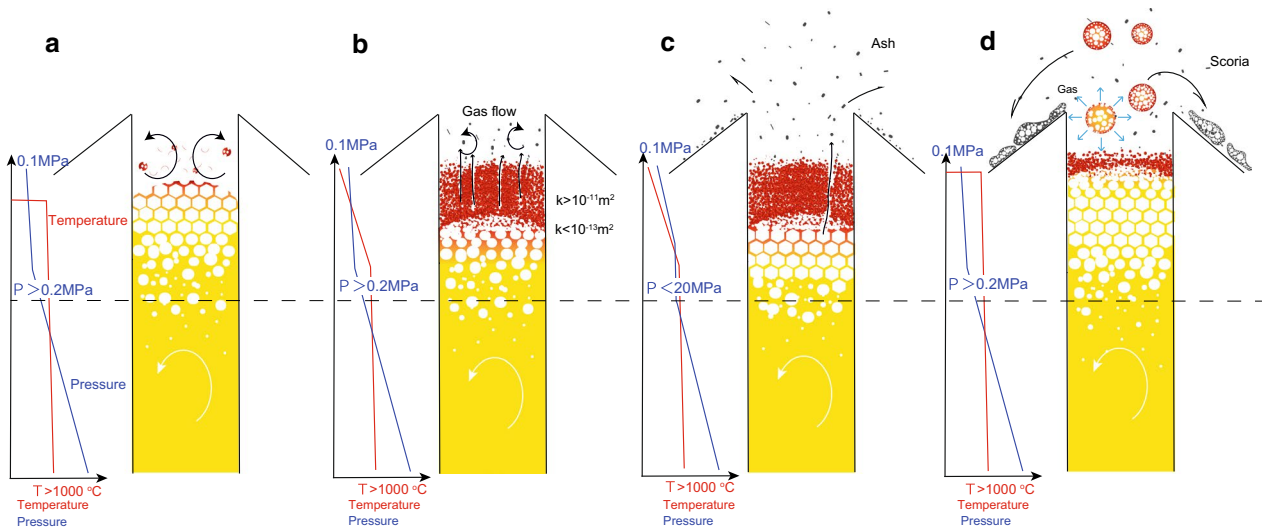


**Fig. 14** Schematic of eruption styles

where $\phi_{\mathrm{open}}$ is the porosity of the pores connected to outside the sample and $r_{\mathrm{cr}}$ is the pore-throat radius, which regulates the flow. In our ash sample, an isolated pore is improbable; thus, $\phi_{\mathrm{open}} \sim \phi_{\mathrm{b}}$. Using $\phi_{\mathrm{b(Compacted)}} = 0.46$, the pore-throat radius explaining the permeability of the sintered ash plate of $2.5 \times 10^{-13}\,\mathrm{m}^2$ is $r_{\mathrm{cr}} = 9\,\mu\mathrm{m}$. In contrast, the throat radius for the powder-like ash layer with a permeability of $4 \times 10^{-10}\,\mathrm{m}^2$ and $\phi_{\mathrm{b(Random)}} = 0.65$ is $r_{\mathrm{cr}} = 130\,\mu\mathrm{m}$, one order of magnitude larger than that estimated for the sintered ash plate. This estimate is consistent with our interpretation; that is, in the powder-like ash layer, particles move to make a pipe-like structure and increase the permeability.

These results show that heating reduces the permeability of the ash layer by reducing the mobility of ash particles. This effect can change the permeability as much as approximately two orders of magnitude.

## Estimated eruptive conditions

In Fig. 14, we summarize the possible conditions in the conduit of Aso Volcano during the eruption in 2014–2015 estimated from our measurements.

The eruption was mainly dominated by ash emission, but sometimes scoriae erupted. Some scoriae showed a high porosity of up to 0.94 and a honeycomb structure (Fig. 2b). The observation of discharged gas amount and the analysis of the melt inclusion indicate that most of the volcanic gas separation occurred in the conduit (Shinohara et al. 2018b). The observed $CO_2/SO_2$ and $SO_2/H_2S$ ratios in the plume on January 12, 2015, during the intensive ash eruption with intermittent Strombolian activity vary from 1.5 to 8 and from 3 to 300, respectively. Here, the ratio of gas compositions depends on the pressure at which bubbles are in disequilibrium with the surrounding melt; that is, bubbles are created or separated from the surrounding melt. The observed $CO_2/SO_2$ and $SO_2/H_2S$ ratios suggest an equilibrium pressure of 0.2–20 MPa (Shinohara et al. 2018b). When the liquid viscosity is sufficiently low, in a conduit with a bubble-generating convection, a foam layer with a honeycomb structure usually develops above a liquid layer, as shown in Fig. 14a (Namiki et al. 2003).

The melt beneath the foam layer convects, but the melt trapped in the foam is not replaced, so that the volcanic gas in the plume above the vent represents the pressure at the bottom of the foam layer, as denoted by the black-dashed line in Fig. 14a–d. Such high-porosity foam does not generate a stress on the liquid-rich layer because of its low density. Thus, the pressure at the dashed line can be close to atmospheric pressure, explaining the estimated low-pressure range of 0.2–20 MPa by gas observations (Shinohara et al. 2018b). The thermal conductivities of foams are usually low, and the foam layer insulates the convecting liquid layer. The temperatures of the magma foam and magma column must approximately be constant. The pressure gradient within the foam layer is quite small, making it difficult to estimate the depth and thickness of the foam layer from the erupted products. On the other hand, the magma head was not observed during the activity. We also cannot estimate the details of the foam from visual observations of the vent.

The top of the foam continuously releases gas inside the bubble into the atmosphere by the rupturing of bubbles or diffusion. Here, the pressures at the top and bottom

of the foam do not vary significantly. Accordingly, the gas compositions in the bubbles do not vary with the depth. In contrast, the uppermost foam is in contact with the cold air and eventually becomes glassy. Our shear deformation measurements show that the fracturing of high-porosity scoriae can occur at a low shear stress $< 10^4$ Pa and a normal stress of $\sim 10^4$ Pa at a low temperature 500 °C (Fig. 7). This stress level is as low as achievable by a large bubble with a length of 0.3 m ascending in a melt with a density of 2700 kg m$^{-3}$. From the viewpoint of the shear rate, a shear rate of 0.005 s$^{-1}$ is sufficient for fracturing, which corresponds to magma ascent at 5 mm s$^{-1}$ in a conduit with a width of 1 m (Fig. 7). The molten magma foam beneath the solidified uppermost foam should ascend continuously. Thus, it is plausible that ash is formed by the fracturing of the magma foam with a high porosity >0.7 at a temperature $\leq 500$ °C (Fig. 8). The observed ash is classified into two types: brownish glass and black particles (Geological Survey of Japan and Kyoto University 2015; Toma et al. 2017). The brownish glass sometimes includes vesicles. Such a glassy ash may be generated by this way.

If there are no rapid gas fluxes, the glassy ash exists above the magma foam as a debris for a while. Even if a large gas emission occurs, some part of the ash can fall back to the vent. For Stromboli Volcano, Italy, the debris generated by fallback of the ash covers the vent and results in a variety of eruption styles and characteristics of ash (e.g., Capponi et al. 2016; D'Oriano et al. 2013; Patrick et al. 2007). Similarly, for Aso Volcano, the ash once emitted from the vent must be cooled by the atmosphere and falls back. The recycled ash accumulating above the magma foam could be sufficiently cold for a while to maintain its granular properties and low friction force, as shown by our deformation experiments (Fig. 10).

Here, by Janssen effect, a column of a granular material does not generate a large load exceeding that scaled with the thickness close to the width of the column (e.g., Duran 1999; Janssen 1895; Roberts et al. 1883). Although there still exist some controversial aspects (e.g., Blanco-Rodriguez and Perez-Angel 2018; Vanel and Clement 1999), this famous behavior of granular material basically arises when the friction coefficient does not depend on the normal stress. In Fig. 9c, the measured friction coefficients of ash at 500 °C do not vary for different normal stresses of 5 and 26 kPa, suggesting that Janssen effect can take place.

Thus, we infer that the pressure at the bottom of this debris layer does not increase significantly, irrespective of its height. The width of the conduit in Aso Volcano is not known. However, the conduit width of Stromboli Volcano whose eruption style is similar to that of Aso Volcano in some part is estimated as several meters (Burton et al. 2007). Thus, the pressure at the bottom of the debris layer should be close to atmospheric pressure. Under such a condition, the force chain sustains the debris layer. The ash particles that are not included in the force chains are movable. Movable ash particles can make pathways for the gas so that the permeability becomes high $k > 10^{-11}$ m$^2$ (Figs. 12, 14b).

Here, we cannot estimate the thickness of the developing debris layer. This is because the bottom of the crater and the magma head are invisible in Aso Volcano, in contrast to those for Stromboli Volcano (Fig. 1d–f). We also cannot characterize the time intervals of the activities. This is because the ash emission of Aso Volcano, which begins gradually without explosions, does not have regularities. As a result, the following discussion becomes qualitative.

Both the black and brown ashes do not show a reddish color, suggesting limited oxidation conditions. This may be because, in the vent area, the entrainment of atmospheric air is low. Even if once the ash is exposed to the atmospheric environment, the timescale must be too short to cause oxidation. In addition, the high temperature in the vent area can obliterate the record of exposure to the atmospheric environment. At a high temperature, the ash changes its texture and color (D'Oriano et al. 2013, 2014). This must be a mechanism for generating the black ash (Toma et al. 2017).

The gas flow in the mobile debris layer causes the collisions of ash particles. Such collisions may not so vigorous but could create ash particles (e.g., Buckland et al. 2018; Dufek and Manga 2008; Kueppers et al. 2012). Small particles reduce the permeability drastically (Koltermann and Gorelick 1995). Eventually, the debris may be reheated by contact with the hot juvenile magma to cause sintering when the temperature exceeds >950 °C and creates a low-permeability layer (Figs. 10, 13). Such a layer can seal the high-pressure volcanic gas to cause subsequent explosions (Fig. 14c). The permeability of the debris layer varies by more than two orders of magnitude by its structure (Figs. 12, 13). If the permeability of the debris layer decreases while maintaining its thickness and the gas flux, the pressure gradient is increased by two orders of magnitude, which is consistent with the pressure variation estimated by gas observation, 0.2–20 MPa (Shinohara et al. 2018b). The loading of debris can also increase the pressure of the magma foam. At a high temperature 950 °C, the debris loses the characteristics of a granular material by sintering (Fig. 9c); thus, Janssen effect disappears, and the debris layer generates a load representing its thickness. If the sintered low-permeability layer locally breaks, it causes the eruption of the materials included in the debris layer and magma foam, which are the

black ash, glassy ash, and volcanic gases generated in the range of 0.2–20 MPa.

As the ash eruption continues, the debris layer becomes thinner so that high-porosity scoriae can erupt (Fig. 14d). The unburied scoriae found at the western rim of the Nakadake 1st crater have low-porosity rims (Fig. 2c). To make such a rim by surface tension-induced shrinkage, our heating experiments suggest that the scoriae erupted at a high temperature (>1000 °C).

The unburied scoriae have a flattened shape. To make the erupted scoriae flatten, flattening has to take place before cooling. The cooling timescale of a scoria with a size of $\lambda$ is approximated as $\lambda^2/\kappa$, where the typical thermal diffusivity of a rock is $\kappa \sim 10^{-6}\,\mathrm{m^2\,s^{-1}}$. The timescale of the relaxation of topography with a horizontal scale of $\lambda$ is expressed as (Turcotte and Schubert 2014)

$$\tau_\mathrm{r} = \frac{4\pi\eta_\mathrm{m}}{\rho_\mathrm{w} g\lambda}, \tag{12}$$

where $\rho_\mathrm{w} \sim 800\,\mathrm{kg\,m^{-3}}$ is the bulk density of the scoria including bubbles and $g = 9.8\,\mathrm{m^2\,s^{-1}}$ is the gravitational acceleration. Applying this formulation to the flattening of scoriae, the topographical relaxation time should be shorter than the cooling timescale, $\tau_\mathrm{r} < \lambda^2/\kappa$. We can constrain the upper limit of the viscosity of the scoria as

$$\eta_\mathrm{m} < \frac{\rho_\mathrm{w} g}{4\pi\kappa}\lambda^3. \tag{13}$$

For scoriae with a size of $\lambda \sim 10\,\mathrm{mm}$, $\eta_\mathrm{m} < 10^3$ Pa s.

This estimate is consistent with the heating experiment shown in Fig. 5. The shrinkage of the scoriae occurs at a high temperature, > 1000 °C, and the viscosity of crystal-free basaltic andesite at ∼ 1000 °C is $\eta_\mathrm{m} \sim 10^3$ Pa s. Although the crystallinity of the scoriae from Aso eruption is high < 0.47, the high porosity of the scoriae may be able to reduce the effect of crystals on the viscosity of the scoria. We thus consider that the pre-eruptive temperature of the scoriae is >1000 °C. We also infer from the heating experiments that the temperature at bubble segregation is >1055 °C (Fig. 5). Fragmentation for an explosive eruption usually occurs when the shear rate is higher than the inverse of the relaxation time of the molten magma (e.g., Gonnermann 2015). The low viscosity of the basaltic andesite ($\eta_\mathrm{m} < 10^3$ Pa s) at a high temperature (>1000 °C) may prevent fragmentation. However, the high-porosity magma foam has elastic properties, which allow the fragmentation of low-viscosity magma to generate scoriae (Namiki and Tanaka 2017).

By removing the low-permeability debris layer, the conduit pressure decreases. Such a pressure reduction allows the inflow of the hydrothermal system (Namiki et al. 2016). The existence of a hydrothermal system beneath the crater floor is evident from the observation of the salt-shell fallout, which is supplied from the gas plume above the dried acid crater lake (1st crater) (Shinohara et al. 2018a). The fluid inflow into the conduit stops the eruption and cools the magma foam. Sudden cooling may be able to fracture bubble walls. This mechanism can effectively generate glassy ash and creates the debris layer again (Fig. 14a, b). The ash emission from Aso Volcano sometimes started without prominent explosions. This observation is consistent with our hypothesis that ash is continuously produced in the conduit.

## Conclusions

The Aso Volcano eruption in 2014–2015 is characterized by ash-dominated eruption and the occasional ejection of high-porosity scoriae. The high-porosity scoriae ($\phi_\mathrm{b} \leq 0.94$) have a low-porosity outer rim and flattened shape, suggesting that the scoriae erupted at a high temperature. We heated the high-porosity scoriae and found that the scoriae at > 1000 °C could shrink to form a low-porosity rim. The deformation experiments show that high-porosity scoriae at a low temperature < 500 °C can easily fracture, even under low shear and normal stresses ∼ $10^4$ Pa. The permeability of the powder-like ash layer is high (> $10^{-11}\,\mathrm{m^2}$), while the fine ash particles at 950 °C are sintered and generate a low-permeability layer (< $2.5 \times 10^{-13}\,\mathrm{m^2}$).

We thus infer the sequence of an eruption as follows. There exists high-porosity magma foam in the conduit. Cooling of the uppermost part of the foam causes fracturing of the magma foam, which creates the glassy brown ash. Some part of the brown ash erupts, and some may fall back into the conduit. If the recycled brown ash remains at the top of the high-temperature foam for long time, it is altered to black ash. The ash particles are initially mobile, and the ash layer has a large permeability. Ultimately, the bottom of the ash layer sinters, and its permeability is reduced. The underlying foam layer is pressurized and ash eruption occurs. Once the debris layer at the top of the magma foam is removed, the underlying magma foam erupts as scoriae.

#### Authors' contributions

AN wrote the paper. YT conducted shrinkage and deformation experiments. TY measured the permeability. All authors read and approved the final manuscript.

#### Acknowledgments

We thank Lucia Gurioli and Michihiko Nakamura for helpful review. We thank Hiroshi Shinohara, Genji Saito, and Akihiko Yokoo for comments, sending us their preprints, and for their help with the field work. We thank Toshiaki Hasenaka for kindly providing scoria samples.

**Competing interests**
The authors declare that they have no competing interests.

**Availability of Data and Materials**
Any additional data and materials are available from AN (e-mail: namiki@hiroshima-u.ac.jp).

**Funding**
This work is supported by Grants-in-Aid for Scientific Research (KAKENHI) 16H04042 and 17KK0092 from the Japan Society for the Promotion of Science (JSPS) to AN.

## Publisher's Note



Received: 28 March 2018 Accepted: 21 August 2018
Published online: 15 September 2018

**References**

Al-Harthi AA, Al-Amri RM, Shehata WM (1999) The porosity and engineering properties of vesicular basalt in Saudi Arabia. Eng Geol 54:313–320
Blackburn EA, Wilson L, Sparks RSJ (1976) Mechanisms and dynamics of Strombolian activity. J Geol Soc 132:429–440. https://doi.org/10.1144/gsjgs.132.4.0429
Blanco-Rodriguez R, Perez-Angel G (2018) Stress distribution in two-dimensional silos. Phys Rev E 97(012):903
Bubeck A, Walker RJ, Healy D, Dobbs M, Holwell DA (2017) Pore geometry as a control on rock strength. Earth Planet Sci Lett 457:38–48
Buckland HM, Eychenne J, Rust AC, Cashman KV (2018) Relating the physical properties of volcanic rocks to the characteristics of ash generated by experimental abrasion. J Volcanol Geotherm Res 349:335–350
Burton MR, Mader HM, Polacci M (2007) The role of gas percolation in quiescent degassing of persistently active basaltic volcanoes. Earth Planet Sci Lett 264:46–60
Capponi A, Taddeucci J, Scarlato P, Palladino DM (2016) Recycled ejecta modulating Strombolian explosions. Bull Volcanol 78:13
Carman PC (1937) Fluid flow through granular beds. Trans Inst Chem Eng 15:150–166
Cashman K, Rust A (2016) Volcanic ash: generation and spatial variations. In: Mackie S, Cashman K, Ricketts H, Rust A, Watson M (eds) Volcanic Ash. Elsevier, Amsterdam, pp 5–22
Chouet B, Dawson P, Ohminato T, Martini M, Saccorotti G, Giudicepietro F, Luca GD, Milana G, Scarpa R (2003) Source mechanisms of explosions at Stromboli Volcano, Italy, determined from moment-tensor inversions of very-long-period data. J Geophys Res 108(B1):2019. https://doi.org/10.1029/2002JB001919
Cigolini C, Coppola D, Yokoo A, Laiolo M (2018) The thermal signature of Aso Volcano during unrest episodes detected from space and ground-based measurements. Earth Planets Space 70:67
D'Oriano C, Pompilio M, Bertagnini A, Cioni R, Pichavant M (2013) Effects of experimental reheating of natural basaltic ash at different temperatures and redox conditions. Contrib Mineral Petrol 165:863–883
D'Oriano C, Bertagnini A, Cioni R, Pompilio M (2014) Identifying recycled ash in basaltic eruptions. Sci Rep 4:5851. https://doi.org/10.1038/srep05851
Dufek J, Manga M (2008) In situ production of ash in pyroclastic flows. J Geophys Res: Solid Earth 113:B09207. https://doi.org/10.1029/2007JB005555
Duran J (1999) Sands, powders, and grains: an introduction to the physics of granular materials. Yoshioka Shoten, Kyoto
Gaudin D, Taddeucci J, Scarlato P, del Bello E, Ricci T, Orr T, Houghton B, Harris A, Rao S, Bucci A (2017) Integrating puffing and explosions in a general scheme for Strombolian-style activity. J Geophys Res: Solid Earth 122(3):1860–1875. https://doi.org/10.1002/2016JB013707
Geological Survey of Japan and Kyoto University (2015) Erupted materials from Aso volcano in November 2014-February 2015. paper presented at meeting of Coordinating Committee for Prediction of Volcanic Eruption (in Japanese). https://www.gsj.jp/hazards/volcano/asokazan2014/index.html
Giordano D, Russell JK, Dingwell DB (2008) Viscosity of magmatic liquids: a model. Earth Planet Sci Lett 271:123–134
Gonnermann HM (2015) Magma fragmentation. Ann Rev Earth Planet Sci 43(1):431–458
Gonnermann HM, Giachetti T, Fliedner C, Nguyen CT, Houghton BF, Crozier JA, Carey RJ (2017) Permeability during magma expansion and compaction. J Geophys Res 122:9825–9848
Gurioli L, Harris AJL, Houghton BF, Polacci M, Ripepe M (2008) Textural and geophysical characterization of explosive basaltic activity at Villarrica volcano. J Geophys Res 113:B08206. https://doi.org/10.1029/2007JB005328
Gurioli L, Colo' L, Bollasina AJ, Harris AJL, Whittington A, Ripepe M (2014) Dynamics of Strombolian explosions: inferences from field and laboratory studies of erupted bombs from Stromboli volcano. J Geophys Res: Solid Earth 119:319–345
Heap MJ, Xu T, Chen C (2014) The influence of porosity and vesicle size on the brittle strength of volcanic rocks and magma. Bull Volcanol 76:856
Houghton BF, Gonnermann HM (2008) Basaltic explosive volcanism: constraints from deposits and models. Chemie der Erde 68:117–140
James M, Bagdassarov N, Müller K, Pinkerton H (2004) Viscoelastic behaviour of basaltic lavas. J Volcanol Geotherm Res 132:99–113
James MR, Lane SJ, Wilson L, Corder SB (2009) Degassing at low magma-viscosity volcanoes: quantifying the transition between passive bubble-burst and Strombolian eruption. J Volcanol Geotherm Res 180:81–88
Janssen HA (1895) Versuche ueber getreidedruck in silozellen. Z Vereins Deutsch Ing 39:1045
Kennedy BM, Wadsworth FB, Vasseur J, Schipper CI, Jellinek AM, von Aulock FW, Hess KU, Russell JK, Lavallee Y, Nichols ARL, Dingwell DB (2016) Surface tension driven processes densify and retain permeability in magma and lava. Earth Planet Sci Lett 433:116–124
Kennedy LA, Russell JK (2012) Cataclastic production of volcanic ash at mount saint helens. Phys Chem Earth 45–46:40–49
Klug C, Cashman KV (1996) Permeability development in vesiculating magmas: implications for fragmentation. Bull Volcanol 58:87–100
Koltermann CE, Gorelick SM (1995) Fractional packing model for hydraulic conductivity derived from sediment mixtures. Water Resour Res 31(12):3283–3297. https://doi.org/10.1029/95WR02020
Kueppers U, Putz C, Spieler O, Dingwell DB (2012) Abrasion in pyroclastic density currents: insights from tumbling experiments. Phys Chem Earth 45–46:33–39
Kumagai H, Lacson R Jr, Maeda Y, Figueroa MS II, Yamashina T (2014) Shallow S wave attenuation and actively degassing magma beneath Taal volcano, Philippines. Geophys Res Lett 41:6681–6688
Kurokawa AK, Miwa T, Okumura S, Uesugi K (2017) Rheology of basaltic ash from Stromboli volcano inferred from intermittent compression experiments. J Volcanol Geotherm Res 343:211–219
Lautze NC, Houghton BF (2007) Linking variable explosion style and magma textures during 2002 at Stromboli volcano, Italy. Bull Volcanol 69:445. https://doi.org/10.1007/s00445-006-0086-1
Lavallee Y, Hirose T, Kendrick JE, De Angelis S, Petrakova L, Hornby AJ, Dingwell DB (2014) A frictional law for volcanic ash gouge. Earth Planet Sci Lett 400:177–183
Leduc L, Gurioli L, Harris A, Colò L, Rose-Koga EF (2015) Types and mechanisms of strombolian explosions: characterization of a gas-dominated explosion at Stromboli. Bull Volcanol 77:8. https://doi.org/10.1007/s00445-014-0888-5
Lindoo A, Larsen JF, Cashman KV, Oppenheimer J (2017) Crystal controls on permeability development and degassing in basaltic andesite magma. Geology 45:831–834
Mangan MT, Cashman KV (1996) The structure of basaltic scoria and reticulite and inferences for vesiculation, foam formation, and fragmentation in lava fountains. J Volcanol Geotherm Res 73:1–18
Marumoto K, Sudo Y, Nagamatsu Y (2017) Collateral variations between the concentrations of mercury and other water soluble ions in volcanic ash samples and volcanic activity during the 2014–2016 eruptive episodes at Aso volcano, Japan. J Volcanol Geotherm Res 341:149–157
Miyabuchi Y, Watanabe K, Egawa Y (2006) Bomb-rich basaltic pyroclastic flow deposit from Nakadake, Aso Volcano, southwestern Japan. J Volcanol Geotherm Res 155:90–103
Miyabuchi Y, ichiro Ikebe S, Watanabe K (2008) Geological constraints on the 2003–2005 ash emissions from the Nakadake crater lake, Aso Volcano, Japan. J Volcanol Geotherm Res 178:169–183

Miyabuchi Y, Iizuka Y, Hara C, Yokoo A, Ohkura T (2018) The September 14, 2015 phreatomagmatic eruption of Nakadake first crater, Aso Volcano, Japan: Eruption sequence inferred from ballistic, pyroclastic density current and fallout deposits. J Volcanol Geotherm Res 351:41–56
Moitra P, Gonnermann HM, Houghton BF, Giachetti T (2013) Relating vesicle shapes in pyroclasts to eruption styles. Bull Volcanol 75:691
Moore PL, Iverson NR, Iverson RM (2008) Frictional properties of the mount St. Helens gouge. US Geol Surv Prof Pap 1750:415–424
Namiki A, Kagoshima T (2014) Intermittent and efficient outgassing by the upward propagation of film ruptures in a bubbly magma. J Geophys Res Solid Earth 119:919–935
Namiki A, Tanaka Y (2017) Oscillatory rheology measurements of particle and bubble-bearing fluids: solid-like behavior of a crystal-rich basaltic magma. Geophys Res Lett 44:8804–8813
Namiki A, Hatakeyama T, Toramaru A, Kurita K, Sumita I (2003) Bubble size distributions in a convecting layer. Geophys Res Lett 30:1784. https://doi.org/10.1029/2003GL01715615
Namiki A, Ueno Y, Hurwitz S, Manga M, Munoz-Saez C, Murphy F (2016) An experimental study of the role of subsurface plumbing on geothermal discharge. Geochem Geophys Geosyst 17(9):3691–3716. https://doi.org/10.1002/2016GC006472
NIED (National Research Institute for Earth Science and Disaster Prevention) et al (2015) Whole-rock chemical composition of essential products collected in the period from December 2014 to January 2015 at Nakadake Crater, Aso volcano. Report of Coordinating Committee for Prediction of Volcanic Eruption (in Japanese). http://www.data.jma.go.jp/svd/vois/data/tokyo/STOCK/kaisetsu/CCPVE/Report/120/kaiho_120_25.pdf
Nishiyama N, Yokoyama T (2017) Permeability of porous media: role of the critical pore size. J Geophys Res: Solid Earth 122(9):6955–6971. https://doi.org/10.1002/2016JB013793
Ohba T, Hirabayashi J, Yoshida M (1994) Equilibrium temperature and redox state of volcanic gas at Unzen volcano, Japan. J Volcano Geotherm Res 60:263–272
Okumura S, Nakamura M, Takeuchi S, Tsuchiyama A, Nakano T, Kentaro U (2009) Magma deformation may induce non-explosive volcanism via degassing through bubble networks. Earth Planet Sci Lett 281:267–274
Okumura S, Uesugi K, Nakamura M, Sasaki O (2015) Rheological transitions in high-temperature volcanic fault zones. J Geophys Res 120:2974–2987. https://doi.org/10.1002/2014JB011532
Ono K, Watanabe K (1985) Geological map of Aso Volcano 1:50,000, vol 4. Geol. Surv, Japan
Ono K, Watanabe K, Hoshizumi H, Ikebe S (1995) Ash eruption of the Nakadake crater, Aso volcano, southwestern Japan. J Volcanol Geotherm Res 66:137–148
Otsuki S, Nakamura M, Okumura S, Sasaki O (2015) Interfacial tension-driven relaxation of magma foam: an experimental study. J Geophys Res Solid Earth 120:7403–7424. https://doi.org/10.1002/2015JB012391
Parfitt EA (2004) A discussion of the mechanisms of explosive basaltic eruptions. J Volcanol Geotherm Res 134:77–107
Patrick MR, Harris AJL, Ripepe M, Dehn J, Rothery DA, Calvari S (2007) Strombolian explosive styles and source conditions: insights from thermal (FLIR) video. Bull Volcanol 69:769–784
Ripepe M (1996) Evidence for gas influence on volcanic seismic signals recorded at Stromboli. J Volcanol Geotherm Res 70:221–223
Roberts I (1883) I. Determination of the vertical and lateral pressures of granular substances. Proc R Soc Lond 36:225–240
Rust AC, Cashman KV (2004) Permeability of vesicular silicic magma: inertial and hysteresis effects. Earth Planet Sci Lett 228:93–107
Schultz RA (1993) Brittle strength of basaltic rock masses with applications to venus. J Geophys Res: Planets 98(E6):10,883–10,895. https://doi.org/10.1029/93JE00691
Sharp RP, Dzurisin D, Malin MC (1987) An early 19th century reticulite pumice from Kilauea Volcano. In: Decker RW, Wright TL, Stauffer PW (eds) Volcanism in Hawaii, U.S. Geol. Surv. Prof. Pap., U.S. Geol. Surv., pp 395–404
Shea T, Houghton BF, Gurioli L, Cashman KV, Hammer JE, Hobden BJ (2010) Textural studies of vesicles in volcanic rocks: an integrated methodology. J Volcanol Geotherm Res 190:271–289
Shinohara H, Matsushima N, Kazahaya K, Ohwada M (2011) Magma-hydrothermal system interaction inferred from volcanic gas measurements obtained during 2003–2008 at Meakandake volcano, Hokkaido, Japan. Bull Volcanol 73:409–421
Shinohara H, Geshi N, Yokoo A, Ookura T, Terada A (2018a) Salt shell fallout during the ash eruption at the Nakadake crater, Aso volcano, Japan: evidence of an underground hydrothermal system surrounding the erupting vent. Earth Planets Space 70:46
Shinohara H, Yokoo A, Kazahaya R (2018b) Variation of volcanic gas composition during the eruption period in 2014-2015 at Nakadake crater. Aso volcano, Japan. https://doi.org/10.1186/s40623-018-0919-0
Sudo Y (2001) The character of volcanic activity at aso volcano: an open system volcano. Chikyu Mon 23:545–550
Taddeucci J, Edmonds M, Houghton B, James MR, Vergniolle S (2015) Hawaiian and Strombolian eruptions. In: Sigurdsson H, Houghton B, McNutt S, Rymer H, Stix J (eds) The encyclopedia of volcanoes, 2nd edn. Academic Press, Amsterdam, pp 485–503
Takeuchi S, Nakashima S, Tomiya A, Shinohara H (2005) Experimental constraints on the low gas permeability of vesicular magma during decompression. Geophys Res Lett 32:L10312. https://doi.org/10.1029/2005GL022491
Terada A, Hashimoto T, Kagiyama T (2012) A water flow model of the active crater lake at Aso volcano, Japan: fluctuations of magmatic gas and groundwater fluxes from the underlying hydrothermal system. Bull Volcanol 74:641–655
Toma T, Nakamura M, Mujin M (2017) What makes volcanic ash black in the ash eruption of the Aso Naka-dake volcano? [abstract]. Bull Volcanol Soc Japan pp A3–25
Turcotte D, Schubert G (2014) Geodynamics. Cambridge University Press, Cambridge
Vanel L, Clement E (1999) Pressure screening and fluctuations at the bottom of a granular column. Eur Phys J B11:525–533
Vasseur J, Wadsworth FB, Lavallee Y, Hess K, Dingwell DB (2013) Volcanic sintering: timescales of viscous densification and strength recovery. Geophys Res Lett 40(21):5658–5664
Vergniolle S, Gaudemer Y (2015) From reservoirs and conduits to the surface, in Hawaiian volcanoes. In: Carey R, Cayol V, Poland M, Weis D (eds) From source to surface. Wiley, Hoboken, NJ
Walker D, Mullins O (1981) Surface tension of natural silicate melts from 1200° C — 1500° C and implications for melt structure. Contr Mineral Petrol 76:455–462
Yokoo A, Miyabuchi Y (2015) Eruption at the Nakadake 1st crater of Aso volcano started in November 2014 (in Japanese). Bull Volcanol Soc Jpn 60:275–278
Yokoyama T, Takeuchi S (2009) Porosimetry of vesicular volcanic products by a water-expulsion method and the relationship of pore characteristics to permeability. J Geophys Res 114:B02201. https://doi.org/10.1029/2008JB005758
Zhu W, Baud P, Wong T (2010) Micromechanics of cataclastic pore collapse in limestone. J Geophys Res 115:B04405. https://doi.org/10.1029/2009JB006610